

AN ABSTRACT OF THE THESIS OF

Natacha Ryckelynck for the degree of Master of Science in Oceanography presented on March 12, 2004.

Title: Understanding the Anodic Mechanism of a Seafloor Fuel Cell

Abstract approved: Redacted for privacy
Clare E. Reimers.

Anoxic sediment overlain by oxic seawater establishes a voltage gradient on the order of 0.7-0.8V across the sediment-water interface. This study follows Reimers et al. (2001) and Tender et al. (2002) who reported the development of a seafloor fuel cell to harvest electrical energy from this potential difference. Prototype fuel cells were deployed for demonstration purposes in the Yaquina Bay estuary, Newport (Oregon, USA) and in a salt marsh near Tuckerton (New Jersey, USA) and were monitored during approximately seven months at either fixed current or fixed potential. Control cells with electrodes not connected to each other (open circuit) were deployed at each site near the prototype devices.

The impacts of fuel cell processes on sediment solids and porewaters were studied by taking cores of sediment down to the surface of the anode (electrode embedded in sediment) of both active and control cells. Porewater profiles showed significant increases in sulfate and iron concentrations, but also sulfide depletion approaching the active anode. Solid-phase acid volatile sulfide and pyrite decreased significantly toward the anode. Fe(III) mineral phases did not appear affected by the presence of the fuel cell. Particulate organic carbon was not depleted significantly either. Electron microprobe analyses and SEM images revealed accumulations of sulfur and iron with Fe/S ratios <1 at the electrode surface of the fuel cell anode. Sulfur deposition was also observed on electrodes simulating a marine fuel cell, under sterile conditions, using HS^- as sole electron acceptor. Moreover current densities and voltages

displayed at both anodes and cathodes in these laboratory experiments were similar to the values measured with the fuel cell devices in the field.

Collectively these results indicate that electron transfer processes at the anodes of seafloor fuel cells result in the oxidation of dissolved and solid-phase forms of reduced sulfur in sediments producing mainly S^0 which deposits at the electrode surface. This oxidation product enhances a localized biogeochemical cycle involving biofilm bacteria that may regenerate sulfate and sulfide. This mechanism may sustain electron transfer processes or co-occur while other biofilm bacteria use the anode directly as a terminal electron acceptor.

© Copyright by Natacha Ryckelynck

March 12th, 2004

All rights reserved

UNDERSTANDING THE ANODIC MECHANISM OF A SEAFLOOR FUEL CELL

by
Natacha Ryckelynck

A THESIS

Submitted to
Oregon State University

in partial fulfillment of
the requirements for the
degree of

Master of Science

Presented March 12, 2004
Commencement June 2004

Master of Science thesis of Natacha Ryckelynck presented on March 12, 2004.

APPROVED:

Redacted for privacy

Major Professor, representing Oceanography

Redacted for privacy

Dean of the College of Oceanic and Atmospheric Sciences

Redacted for privacy

—

Dean of the Graduate School

I understand that my thesis will become part of the permanent collection of Oregon State University libraries. My signature below authorizes release of my thesis to any reader upon request.

Redacted for privacy

Natacha Ryckelynck, Author

ACKNOWLEDGEMENTS

First of all, I cannot start this section without expressing my gratitude to Clare Reimers, my major advisor, that gave me the opportunity to work on this fascinating project. I learned a lot working with her; she provided the guidance that allowed me to accomplish this work.

I could not have done all this work without the help of Jody Stecher. He managed the work prior and during the sampling: he ensured the continuous operation of the devices, organized and took part in the dives, participated in the field work (in Yaquina Bay and in Tuckerton), and processed the two cores for the porewater analyses. He assisted me in my lab work. Thanks to him I also discovered the *wonderful world* of microelectrodes. His pluridisciplinary skills made the work in the lab in Newport much easier.

Other laboratory assistance in Corvallis was given by Chi Meredith, Katherine Brooksforce and Andy Ross who ran some of the analyses (manganese, dissolved iron, ammonia, phosphate, silicate, sulfate and chloride), and Margaret Sparrow who helped me to analyze for solid carbon and nitrogen.

I am grateful to Dr. Roger Nielsen, Ed Kohut and Mike Rowe for helping me to prepare and analyze my SEM - electron microprobe samples, and for providing comments and advice for the results interpretation.

Thank you to M. Sommer, R. Emmett, T. Bridgeman, T. Builder, W. Hanshumacher, D. Jacobson and M. Spencer for diving assistance, that made possible the prototypes deployment, the sediment sampling, and the technical assistance with the devices.

I would like to acknowledge Leonard Tender for the installation and operation of the Tuckerton device, and for organizing its recovery and associated sampling. Daniel Lowy, Dawn Holmes, Daniel Bond, Kanoeli Pilobello and Andy Ross also participated in the recovery and the sediments sampling of either the Oregon or the New Jersey devices.

Suggestions and encouragements offered by Martin Fisk, Anna-Louise Reysenbach and Erik Larson, my committee members, were very valuable in the completion of my thesis.

Being a graduate student in an university in the United States means a lot for me. It was a professional and also a personal enrichment. As part of this process, I want to thank my professors for all what I learnt by assisting to their classes and meeting with them, and for their efforts in improving my knowledge with always new and interesting subjects. I really appreciated to be part of the COAS student community, which helped me to go through my student life.

I really enjoyed spending time with Roberto and Amy, having dinner and watching movies together. Babysitting Aidan was also a fun activity.

Special thanks to my roommates Jennifer Burke, Mark Nielsen, Christopher Wolfe, Ida Royer, and Rachel Sanders, who made me feel at home and provided their daily support.

The support of my family and my friends in France (or in Europe and elsewhere in the World) was very precious, despite the distance between us.

Le Cercle, with its daily meeting at the Interzone (on Monroe) for a coffee and a piece of coffee cake, its lunch "a la patate chaude" and others, was an essential part of my journey as a Graduate Student in Corvallis.

Thank you to Marianne, too, for our long discussions during coffee breaks watching the Pacific Ocean in Newport and for the relaxing week ends at her place. Her presence was very supportive during my journey in Oregon.

This work was supported by the Office of Naval Research and DARPA. The U.S. National Science Foundation supported my graduate research assistantship while I prepared my thesis.

TABLE OF CONTENTS

	<u>Page</u>
I. INTRODUCTION	1
II. EXPERIMENTAL APPROACH.....	6
II.1. Fuel cells.....	6
II.2. Sample collection.....	8
II.2.a. Sediment sampling	8
II.2.b. Anode sampling.....	9
II.3. Porewater extraction	11
II.4. Porewater analyses.....	11
II.5. Solid phase analyses	13
II.6. Laboratory simulations of the marine fuel cell under sterile conditions ..	15
II.7. Electron microprobe analyses and SEM images.....	18
III. RESULTS	20
III.1. The fuel cell	20
III.2. Sediment geochemistry	23
III.3. Anode surfaces.....	32
III.4. Laboratory simulations	37
IV. DISCUSSION.....	45
IV.1. Electron transfer to the anode: microbial and/or electrochemical	45
IV.2. Electrochemical oxidation of sulfide	47
IV.3. Electrochemical reactivity of sulfide minerals	48
IV.4. Elemental sulfur as an oxidation product.....	49
IV.5. Other chemical consequences of sulfide mineral oxidation	51
IV.6. Consequences of sulfur deposition	51
IV.7. Biogeochemical cycle of sulfur	53
V. CONCLUSION.....	56

TABLE OF CONTENTS (Continued)

VI. BIBLIOGRAPHY..... 58

APPENDICES 65

LIST OF FIGURES

<u>Figure</u>	<u>Page</u>
1. Schematic redox mechanism of the seafloor fuel cell.	3
2. Picture of the Yaquina Bay device before deployment.	7
3. Color differences between sediment that was in contact with the electrode surface (light brown) and sediment from further above in the sediment column (dark).	10
4. Picture of the two chambers used for the laboratory simulations.....	16
5. Whole cell potential (cathode - anode) (a), anode potential (anode - reference) (b), cathode potential (cathode - reference) (c), current density (d) and power density (whole-cell potential x current density) (e) recorded during the seven-month experiment in the Yaquina Bay Estuary.	21
6. Porewater profiles associated with the experiment in Yaquina Bay Estuary.	24
7. Sulfide profiles of sediment cores from the Yaquina Bay experiment, measured by voltametry.....	25
8. Solid phase profiles associated with the experiment in Yaquina Bay Estuary.....	27
9. Porewater profiles associated with the experiment in the Tuckerton salt marsh.....	29
10. Solid phase profiles associated with the experiment in Tuckerton NJ salt marsh...	31
11. BSE images of surface cross-sections of graphite electrodes that were buried in Yaquina Bay.	33

LIST OF FIGURES (Continued)

12. Spatial elemental analysis by X-ray mapping of the distribution of iron (b), oxygen (c) and sulfur (d) on a cross-section of the active anode from the Yaquina Bay experiment. The BSE image (a) refers the elemental maps to the different phases present at the electrode surface. Accumulation of white dots indicate higher elemental concentration. 34
13. Electron microprobe profiles across the interface of the graphite anode deployed in the Yaquina Bay Estuary (Oregon)..... 36
14. Sulfur (a) and iron (b) transects along the interface of a piece of the anode deployed in the Yaquina Bay Estuary (Oregon), compared to the reference sample (unused graphite). 38
15. Fe/S atomic ratio as function of the iron content at the electrode surface between graphite and biofilm for the fuel cell anode..... 39
16. Variations of the anode potential (vs. Ag/AgCl) (a) and current density (b) during the laboratory simulations, run for 6 days. 41
17. BSE images (a, b) and spatial distribution of S (c, d) (by X-ray map) on surface cross- sections of anode pieces from the laboratory simulations. 43
18. Comparison of sulfur deposition between the open circuit and the energy harvesting experiments..... 44
19. Biogeochemical cycle amplified by the fuel cell mechanism. 54

LIST OF APPENDICES

<u>Appendix</u>	<u>Page</u>
A. Integration of the concentration gradients and conversion to moles of electrons ..	66
B. Elemental sulfur deposition.....	70
C. Porewater data from the Yaquina Bay experiment.....	72
D. Solid-phase data from the Yaquina Bay experiment.....	75
E. Porewater data from the Tuckerton experiment.....	78
F. Solid-phase data from the Tuckerton experiment	79
G. Electron microprobe profiles of the active anode surface.....	80
H. Electron microprobe measurements along the surfaces of active and control electrodes, and Fe/S ratios.....	83

UNDERSTANDING THE ANODIC MECHANISM OF A SEAFLOOR FUEL CELL

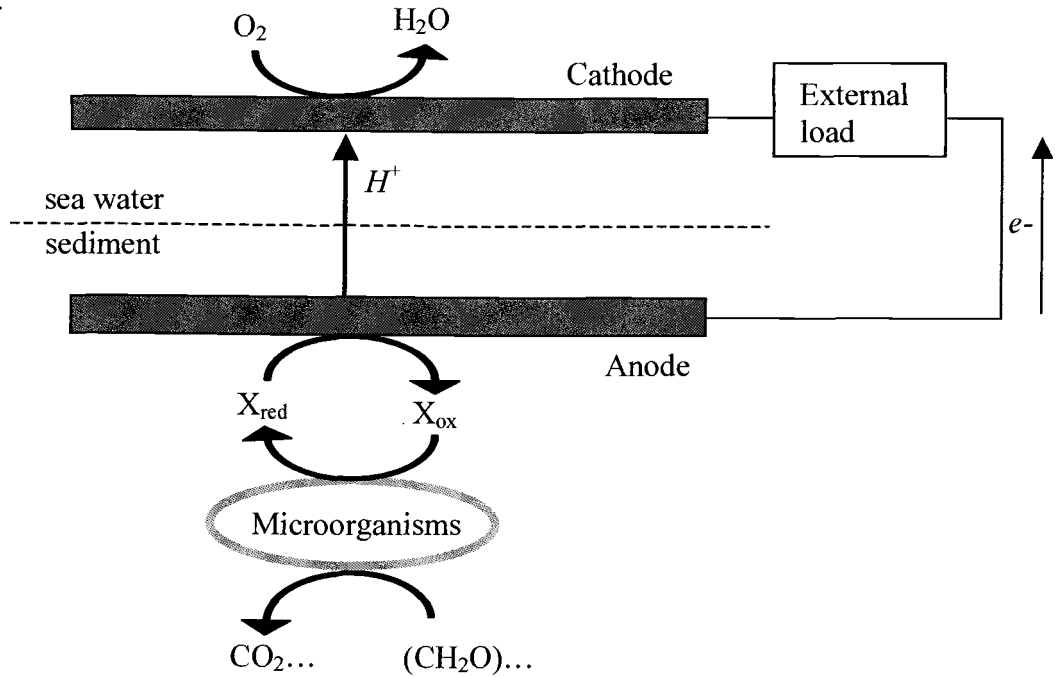
I. INTRODUCTION

Primary production in surface waters of the ocean regulates the deposition of organic matter on the seabed. In highly productive areas (coastal zones and continental margins), organic carbon may accumulate at rates of 0.05 - 40 gC/m²/y (MULLER and SUESS, 1979; WALSH et al., 1985) creating sediments containing 0.5 - 20 weight % C_{org} (CANFIELD, 1989a; CANFIELD, 1989b; JØRGENSEN, 1977; KEIL et al., 1994; MULLER and SUESS, 1979; RANSOM et al., 1998; WALSH et al., 1985). This organic matter fuels aerobic and anaerobic microbial respiration depleting the sediment of dissolved oxygen and enhancing the activity of sulfate-reducing bacteria (BERNER, 1978; CANFIELD, 1989a; GOLDHABER and KAPLAN, 1975; JØRGENSEN, 1977; JØRGENSEN, 1982; LIN and MORSE, 1991). Sulfide produced by sulfate-reducing bacteria and abiotic reactions may react with sedimentary iron to form a variety of iron-sulfide minerals, including amorphous-FeS, mackinawite FeS_(1-x), greigite Fe₃S₄, and pyrite FeS₂ (BERNER, 1970; BERNER, 1984; BERNER, 1985; GOLDHABER and KAPLAN, 1975; LIN et al., 2002; LIN and MORSE, 1991; WANG and MORSE, 1996). Experimental investigations have indicated that amorphous-FeS, FeS_(1-x), and Fe₃S₄ are generally only present in recent sediments and act as metastable intermediates (WANG and MORSE, 1996) in the formation of pyrite (BERNER, 1964). Accumulation of sulfides fixes the Eh of a marine sediment at a potential on the order of 0.6-0.8V lower than overlying oxic seawater (BAAS BECKING et al., 1960; BERNER, 1963; JØRGENSEN and FENCHEL, 1974). Reimers et al. (2001) and Tender et al. (2002) have investigated tapping into this potential difference to convert chemical energy to electrical energy using the principles of a fuel cell. Fuel cells, unlike batteries, are electrochemical devices continuously fed with electroactive compounds stored outside the cell (BACON and FRY, 1970; GREAVES, 1970; MCDUGALL, 1976; VIJH, 1970). A seafloor fuel cell consists of an electrode buried in anoxic sediment (anode) and connected to another electrode positioned above

in seawater (cathode) (figure 1). Dissolved oxygen present in bottom seawater is supplied as oxidant to the cathode, while the anode is in contact with local dissolved and solid-phase reductants. Reactions occurring at the anode surface have not yet been fully identified, but the rate of transfer of reduced species from the sediment appears to provide an upper limit to the overall rate of electrochemical reaction. Preliminary results (TENDER et al., 2002) suggested that sulfide oxidation to elemental sulfur can be the dominant source of electrons to the anode. This mechanism is consistent with previous studies demonstrating electrochemical oxidation of sulfide under a wide range of environmental and laboratory circumstances (ATEYA and ALKHARAFI, 2002a; ATEYA and ALKHARAFI, 2002b; ATEYA et al., 2003; CASTANEDA et al., 1987; SHIH et al., 1989). Bacteria are also suspected to play an important role in the seafloor fuel cell mechanism, reducing by-products generated by electrochemical reactions at the anode (e.g. S^0 , SO_4^{2-}), or using the anode as a terminal electron acceptor. These mechanisms are consistent with descriptions of different electron transport pathways within biofilms (HERNANDEZ and NEWMAN, 2001; NEVIN and LOVLEY, 2002). Some microbes with outer membrane-bound enzymes establish direct contact (BELIAEV and SAFFARINI, 1998; BELIAEV et al., 2001; GASPARD et al., 1998; MAGNUSON et al., 2000; MYERS and MYERS, 1992; NEVIN and LOVLEY, 2000), while others may transfer electrons via extracellular compounds that are already present in the environment (LOVLEY et al., 1996; NEVIN and LOVLEY, 2000; SCOTT et al., 1998; STRAUB et al., 2001) or microbially generated (NEVIN and LOVLEY, 2000; NEVIN and LOVLEY, 2002; SEELIGER et al., 1998; STRAUB et al., 2001).

To develop a better understanding of the mechanism(s) of electron transfer to anodes in marine sediments, this study examines the effects of seafloor fuel cell reactions on surrounding sediments and on the surface properties of the electrodes. Samples for this work were collected in association with deployments of prototype seafloor fuel cells in the Yaquina Bay estuary, Newport (Oregon, USA) and in a salt marsh near Tuckerton (New Jersey, USA) (TENDER et al., 2002). These field experiments had been monitored during approximately seven months at either fixed current or fixed potential, and scrapings of the anode surfaces were taken to characterize

Figure.1: Schematic redox mechanism of the seafloor fuel cell as described by Reimers et al. (2001). Reduced species produced by microbial decomposition of organic matter are oxidized at the anode; electrons and protons are transferred to the cathode and utilized in the reduction of dissolved oxygen to water in oxic bottom water.



microorganisms enriched by fuel cell processes (table 1) (HOLMES et al., in press; TENDER et al., 2002). The salt marsh anode was found to be colonized to a large extent by bacteria related to *Desulfuromonas acetoxidans*, a member of the *Geobacter* family within the delta-Proteobacteria group. These microorganisms are known to use Fe(III) (RODEN and LOVLEY, 1993) and elemental sulfur (PFENNING and BIEBL, 1976) as electron acceptors in the oxidation of organic matter. The same electrode showed a secondary enrichment in species from the *Desulfobulbus/Desulfocapsa* genera. These microbes also belong to the delta-Proteobacteria group and are known to disproportionate elemental sulfur (FINSTER et al., 1998; LOVLEY and PHILLIPS, 1994). The primary bacterial enrichment on the anode of the fuel cell operated in the estuarine sediment was related to the *Desulfobulbus/Desulfocapsa* cluster. An increase of bacteria in the cytophagales group was also observed on the same electrode. These organisms are generally characterized as fermenters able to break down macromolecules. Part of the motivation for this study was to relate the selectivity of the fuel cell for groups of bacteria to chemical conditions at and feeding into the anode.

Microbial enrichment and harvested energy have been suggested to be dependent on the geochemistry of sediments surrounding the anode (REIMERS et al., 2001; TENDER et al., 2002). Therefore sediments impacted by the fuel cell were characterized for a variety of potentially influential constituents present in porewater and solid-phases. A particular emphasis was placed on sulfide species and organic C because on a mass basis, these materials are the most abundant reductants present in coastal environments. Laboratory simulations of the fuel cell were also run under sterile conditions using only dissolved sulfide as an electron source. To complete these investigations, anode samples from both field experiments and laboratory simulations were analyzed by scanning electron microscopy and electron microprobe to provide indications of the elements reacting at the electrode surface.

Table 1: Percentage of the major phylogenetic groups of bacteria identified from 16S rDNA sequences recovered from the anodes of the active and the control cells deployed in the Tuckerton salt marsh (New Jersey) and in the Yaquina Bay estuary (Oregon), from Tender et al. (2002) and Holmes et al. (in press).

<u>Bacterial group</u>	<u>Related genera</u>	<u>Estuary</u>		<u>Salt marsh</u>	
		Fuel cell	Control cell	Fuel cell	Control cell
α-Proteobacteria		-	7.1%	3%	17%
δ-Proteobacteria	<i>Desulfobulbus spp./</i>	62.5%	11.9%	24%	1%
	<i>Desulfocapsa spp.</i>	-	-	45%	9%
	<i>Desulfuromonas spp.</i>	-	23.8%	7%	13%
	<i>sulfate reducing</i>	-			
ε-Proteobacteria		-	-	-	3%
γ-Proteobacteria		-	16.5%	9%	21%
Cytophagales		32.5%	9.5%	5%	6%
other bacteria		5%	28.6%	7%	30%

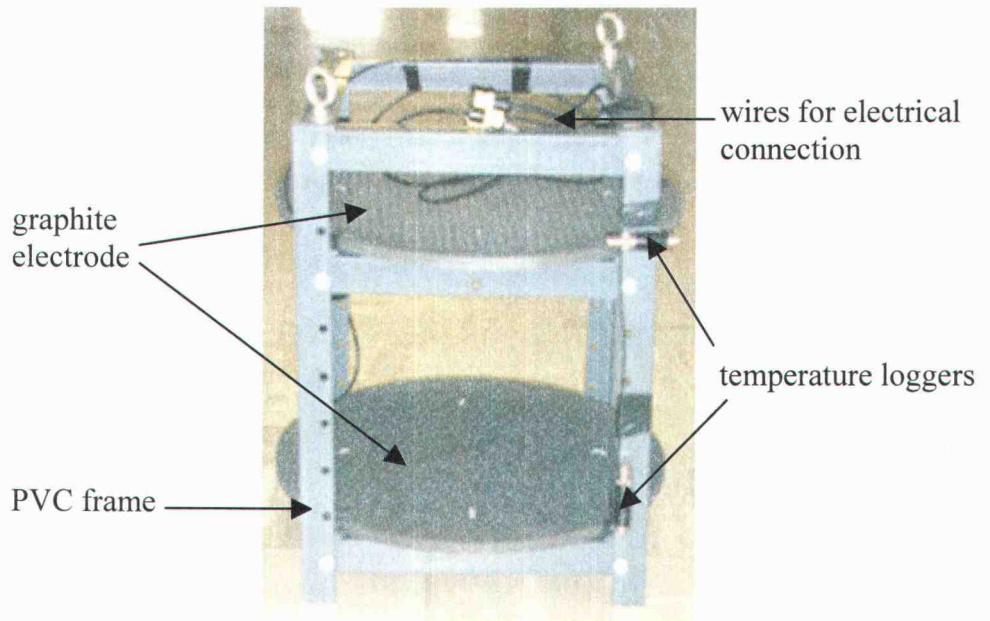
II. EXPERIMENTAL APPROACH

II.1. Fuel cells

The prototype fuel cells deployed prior to the analyses in this study were fabricated from two 48.3 cm diameter x 1.3 cm thick graphite discs (LG graphite grade 10, Graphite Engineering and Sales, Greenville, MI) serving as electrodes and connected to a programmable resistive load (870, Scribner Associates, Southern Pines, NC) as described in Tender et al. (2002). The electrode surface area was 0.567 m² (Appendix A). Anodes and cathodes were positioned parallel to and from 10-20 cm below and above the sediment-water interface, respectively. At each site, a control cell with unwired electrodes (open circuit) was also deployed a few meters from the energy-harvesting device. The electronic device monitored the whole-cell potential (cathode vs. anode), half-cell potential (a bare Ag/AgCl reference electrode vs. anode) and current during the length of each experiment. These parameters were used to calculate the anode potential (anode vs. reference electrode), the cathode potential (cathode vs. reference electrode) and the electrical power (whole-cell potential x current). Current and power were normalized to the surface area.

In the case of the New Jersey experiment, active and control devices were enclosed within 167 L cylindrical PVC containers partially filled with approximately 50 L of sediment (TENDER et al., 2002). An acrylic disc the diameter of the container was placed on top of the sediment to facilitate the separation of anode and cathode compartments. Interactions with the marine environment were limited to water exchange across 80 screened circular openings (5.1 cm diameter) throughout the container walls. These openings were distributed in five rows of 16 holes each; two lines of screens were positioned at the anode level and the three others were located at the top of the container. In contrast, the electrodes deployed at the Oregon estuarine site were fixed 30.5 cm apart within an open PVC frame that was partially buried (figure 2). This configuration allowed this experiment to be influenced by a full range of environmental processes, including new sedimentation, sediment bioturbation, and tidal exchanges of bottom water. Two sub-miniature temperature recorders (MDS Mark V/T,

Figure 2: Picture of the Yaquina device before deployment.



Alec Electronics Co., Kobe, Japan) where positioned next to the cathode and the anode of the active device (figure 2) and measured seawater and sediment temperature, respectively.

II.2. Sample collection

II.2.a. Sediment sampling

After deployments of approximately seven months, experiments were recovered from the Tuckerton salt marsh (water depth 1 - 2 m) on August 7th and 8th 2001, and from the Yaquina Bay estuary (water depth 5 - 6 m) on January 26th and 28th 2002. The salt marsh fuel cells and surrounding sediments were sampled after lifting the containers onto an adjacent boat dock with a small boat's winch. The Yaquina Bay experiments required SCUBA divers to retrieve both the fuel cells and surrounding sediments.

Tuckerton Sampling: The PVC containers were opened on the dock and the cathodes removed first. Then the overlying water was drained with a siphon, and the sediments exposed by removing the acrylic separator. Duplicate core tubes (8 cm ID) were inserted immediately down to the anode surface and capped. These cores were then retrieved by sliding thin acrylic sheets under each tube, and removing sheet and core to a N₂-filled glove bag at 25±3°C in an adjacent field-station laboratory. Meanwhile, the anode was fully uncovered and removed for microbiological sampling (see below). A second set of cores was taken of the underlying sediment and also removed to the laboratory.

Yaquina Bay Sampling: To remove sediment cores from above the active fuel cell anode in the estuary, divers removed first the cathode from the PVC frame and brought it to the surface. Then they inserted three core tubes into the sediment down to the anode and capped them. A first core was taken to the surface and later discarded. The frame was removed from the seafloor while maintaining the sediment and the two remaining core tubes intact on the anode. Once on the dock, these cores were handled similarly to the cores retrieved from the Tuckerton experiment and were transferred to a laboratory cold room at 10°C. In addition, after the cores were pulled, the entire anode

(still covered with sediment) was removed to the laboratory cold room and placed under nitrogen for further sampling.

Sediment sampling in proximity to the Yaquina Bay control cell had to be conducted differently due to poor visibility and difficult diving conditions. Two sediment cores were taken directly along side the fuel cell as close to the anode and cathode as possible. These cores extended from the sediment-water interface down to about 5 cm below the anode. The whole device was then removed and taken to the dock where it was disassembled. A third core (without any overlying water) was taken while the sediment column was still intact on the anode and was transported immediately to the 10°C cold room. The anode with remaining sediment was then transferred to a glove bag under nitrogen for additional sampling.

II.2.b. Anode sampling

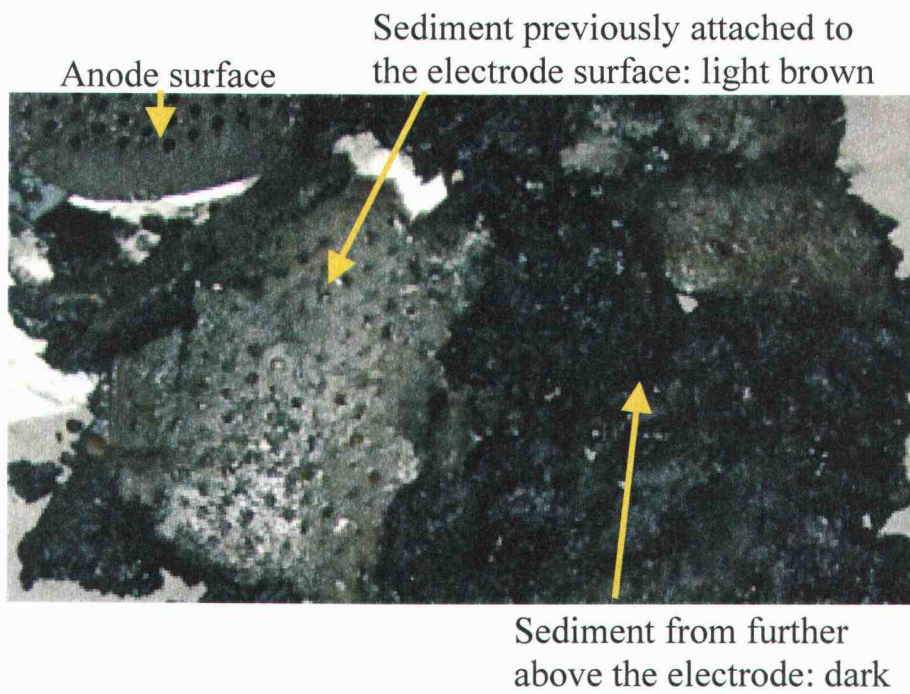
Sediments directly in contact with the active anodes from both sites were observed to be lighter in color than overlying sediment layers (figure 3). In order to document chemical reasons for this color change, two samples of the first 1 cm of sediment directly covering sections of the Yaquina Bay active anode were removed and set aside in centrifuge tubes while under N₂.

Then pieces of exposed graphite surface from active and control anodes¹ were cut off with a saw and immediately frozen in order to minimize surface reactions through oxidation or bacterial activity. These graphite samples were stored at -45°C under nitrogen for later surface analysis.

Other areas of the anode surfaces from both the New Jersey and Oregon experiments were carefully washed with sterile artificial seawater and scraped with a sterile razor blade into 1.5 ml TE buffer (pH 8; Sigma, St Louis, MO). These samples were then frozen for microbial 16S rDNA analysis following the procedures described in Tender et al. (2002) and in Holmes et al. (in press).

¹ Yaquina Bay experiment only

Figure 3: Color differences between sediment that was in contact with the electrode (light brown) and sediment from further above in the sediment column (dark).



II.3. Porewater extraction

One core from each set collected either above, below or along the anodes of the active and control cells was selected for sectioning and porewater extraction. Overlying water when present was subsampled into a 50 mL centrifuge tube and treated the same as a sediment sample. Then the remaining overlying water was removed with a syringe, and the cores placed on an extruder under N₂ in a glove bag.

Sediment was sliced into 0.5 - 2.0 cm sections using a stiff beveled plastic sheet ca. 1 mm thick. The outer 0.5 cm of each sediment slice was discarded to minimize edge artifacts, and the remainder was homogenized with a plastic spatula and transferred into acid-washed centrifuge tubes and capped. Some sample intervals were separated into two samples that were analyzed individually. The two extra samples collected directly from the Oregon anode surface were processed as core slices. Porewater was separated from the sediment by centrifuging at environmental temperatures at 8,000 rpm for 10 minutes. Samples were collected in a clean glove bag under nitrogen by decanting the porewater into acid-washed syringes fitted with 0.45 µm Supor® syringe filters (Gelman). The filtered water was subsampled for various analyses. Centrifuge tubes containing the sediment were resealed, and stored in N₂-filled bags at -45°C for later analysis.

II.4. Porewater analyses

- Sulfide: Aliquots of filtered porewater were immediately analyzed for total dissolved sulfide (i.e., H₂S + HS⁻ + S²⁻ although the species HS⁻ is dominant in seawater at pH 6 - 8) using a method modified from Cline (1969). Porewater subsamples were drawn under a N₂ atmosphere and then mixed with diamine reagent concentration "C", diluted after full color development, and detected by spectrophotometry at 670 nm. Standard solutions were made from Na₂S·9H₂O crystals (reagent grade, Fisher scientific, Fair Lawn, NJ) dissolved in N₂-purged de-ionized water.

Duplicate cores were used to measure profiles of sulfide with fine spatial resolution by voltammetry (BRENDEL and LUTHER III, 1995; LUTHER III et al., 1998; ROZAN et al., 2000). Measurements were performed with a 3-electrode system connected to a potentiostat (Model DLK100, Analytical Instrument System Inc,

Flemington, NJ). A mercury-drop microelectrode was used as working electrode (BRENDL and LUTHER III, 1995; LUTHER III et al., 1999), and potentials were measured versus a Ag/AgCl reference electrode while current was passed through a platinum counter electrode. Mercury-drop microelectrodes consisted of 100 μm diameter gold wire inserted into 200-800 μm diameter glass capillaries and sealed with epoxy. The electrode tip was polished with fine abrasive paste (METADI SUPREME polycrystalline diamond suspensions, Buehler LTD, Lake Bluff, IL) and electrochemically plated for 4 min at -0.1 V (vs. Ag/AgCl electrode) with 0.1 mol/L $\text{Hg}(\text{NO}_3)_2$ in 0.05 mol/L HNO_3 solution; this reaction formed a mercury drop amalgamated with Au. Sulfide peaks were measured by cyclic voltammetry. Potentials were scanned from -0.1 V to -1.8 V at a rate of 1000 mV/sec; a conditioning step was set at -0.8 V for 30 sec before measurements to remove iron, manganese and sulfide deposited on the electrode, and the potential was held at this value in between scans. Microelectrodes were calibrated under continuous N_2 flow by successive 100 μL additions of 20.8 mM Na_2S solution into 50 mL O_2 -free seawater. Depth measurements were controlled by a custom-built micro-manipulator (CMPT Inc., Lewes, DE).

- Iron and manganese: Samples for iron and manganese² (1.0-1.5 mL) were acidified with 10 μL 3.0 M HCl (TraceMetal Grade, Fisher Scientific) and analyzed after appropriate sample dilution by separate flow injection analysis methods adapted from Measures et al. (1995) and Resing and Mottl (1992). The analytical procedures are based on a colorimetric reaction. In an acidified solution iron catalyses the oxidation of N,N-Dimethyl-p-phenylenediamine (DPD) by hydrogen peroxide. The product of this reaction has a red-purple color which can be detected spectrophotometrically at 541 nm. Similarly, Mn can be quantified through its catalytic effect on the formation of malachite green by reaction of leucomalachite green with sodium periodate. The absorption maximum for malachite green is at 620 nm. The amounts of oxidized DPD and produced malachite green are proportional to the amounts of iron and manganese, respectively. The detection limits are on the order of 0.5 nM for Fe^{2+} and 0.05 nM for Mn^{2+} .

² Yaquina Bay experiment only.

- Sulfate and chloride: Sulfate and chloride were determined after dilution of unacidified samples using a DX-500 ion chromatograph equipped with a GP40 pump, a LC25 chromatography oven, an AG14 column, ED40 electrochemical detector, and a AS40 autosampler (Dionex, Sunnydale, CA). Samples were eluted with a 3.5 mM $\text{Na}_2\text{CO}_3/1.0$ mM NaHCO_3 solution, using argon as carrier gas. The system pressure was ca. 5 psi and the furnace temperature set at 30°C.

- Nutrients: Silicate, phosphate and ammonium were determined using a nutrient autoanalyzer (Alpkem, Clackamas, OR) after appropriate dilution of unacidified filtered porewater samples. It was noted that some of the Yaquina Bay porewater samples appeared yellow and cloudy when exposed to air before the nutrient subsamples were drawn. Later analyses revealed that these samples had high dissolved iron concentrations.

II.5. Solid phase analyses

A subset of samples that had been processed for porewater chemistry was selected for solid phase analyses. Prior to chemical extraction procedures, centrifuge tubes containing the sediment solids were thawed overnight under N_2 . Each sample was homogenized before subsampling. Wet/dry weight ratios were determined for each sample by weighing 0.5 to 1 g wet sediment in triplicate in pre-weighed aluminum cups and drying these at 75°C to a constant dry weight. These ratios were later used to normalize iron and sulfur mineral contents extracted from weighed wet samples to a dry weight of sediment.

- Iron oxides: Iron oxides in amorphous and crystalline forms were extracted separately, under nitrogen in a glove box. The two extractions were run in parallel in triplicate for each sample. Oxygen-free reagents were freshly prepared before the extractions. Crystalline iron oxides (hematite, goethite, magnetite) reacted with a solution of dithionite (0.83 g sodium dithionite dissolved in 20 ml of 0.5 M sodium citrate/0.35 M acetic acid): a N_2 -purged centrifuge tube containing 0.5 - 1 g wet sediment was filled with 20 mL of extracting solution and placed on a shaker for four hours at 60°C (KOSTKA and LUTHER III, 1994; WIJSMAN et al., 2001). Amorphous iron oxides ($\text{Fe}(\text{OH})_3$, ferrihydrite) were determined by shaking 0.5 - 1 g wet sediment in 20

mL ascorbate solution (ascorbic acid 22 g/L in 0.5 M sodium citrate/0.25 M sodium bicarbonate) for 24 hours at room temperature (FELDERMAN et al., 1991; KOSTKA and LUTHER III, 1994). Vials were centrifuged 10 min at 8000 rpm at 8°C; extracts were filtered under N₂ atmosphere with 0.45 µm Acrodisc® syringe filters (Gelman) and acidified with 100 µL 6 N HCl (trace metal grade, Fisher Scientific, Fair Lawn, NJ). Dilution factors of 1:100 and 1:10 were applied to aliquots of the crystalline and amorphous Fe extracts, respectively, before measuring iron concentrations by spectrophotometry using ferrozine (STOOKEY, 1970). Volumes of 0.1 mL of reducing agent (15 g hydroxylamine hydrochloride dissolved in 150 mL 6 N HCl), 0.1 mL ferrozine (5.1 g/l) and then 0.1 mL buffer (60 g ammonium acetate dissolved in 52.5 mL ammonium hydroxide, diluted to 150 mL) were added successively to 5 mL diluted samples. Each reagent addition was separated by 30 min to allow complete reaction, and samples were vortexed after each addition. Absorbances were read at 562 nm. Standards were prepared using electrolytic iron powder < 100 mesh (Fisher scientific, Fair Lawn, NJ) dissolved in 0.6 N HCl and treated in the same way as extracted samples.

-Solid sulfides: Reduced sulfur species in the form of pyrite (FeS₂) and acid volatile sulfides (AVS) (which include metastable solid sulfides, mainly iron-monosulfide FeS) were analyzed by a sequential scheme under a continuous flow of nitrogen. Starting with triplicate subsamples, AVS present in 0.2 - 0.5 g wet sediment was extracted for two hours by acid distillation (15 ml 1 N de-oxygenated HCl) under boiling conditions (ALLEN and PARKES, 1995; ZHABINA and VOLKOV, 1978). The liberated H₂S was stripped from the solution with N₂ gas and trapped into a known volume (10 - 20 mL) of 1 M zinc acetate: H₂S reacts with Zn(Ac)₂ to form a ZnS precipitate stable under oxic conditions. Pyrite was distilled directly at the end of AVS extraction using the Cr(II) reduction method (CANFIELD et al., 1986; FOSSING and JØRGENSEN, 1989; WIJSMAN et al., 2001). This second extraction also includes the reduction of elemental sulfur to H₂S. AVS traps were replaced by new traps containing 40 ml of 1 M Zn(Ac)₂ de-aerated with N₂. De-oxygenated reagents (16 ml 1 N CrCl₂ in 0.5 N HCl and 8 ml concentrated HCl) were slowly added. Distillation proceeded first at room temperature for 15 min, followed by 45 min under a gentle boil. CrCl₂ was

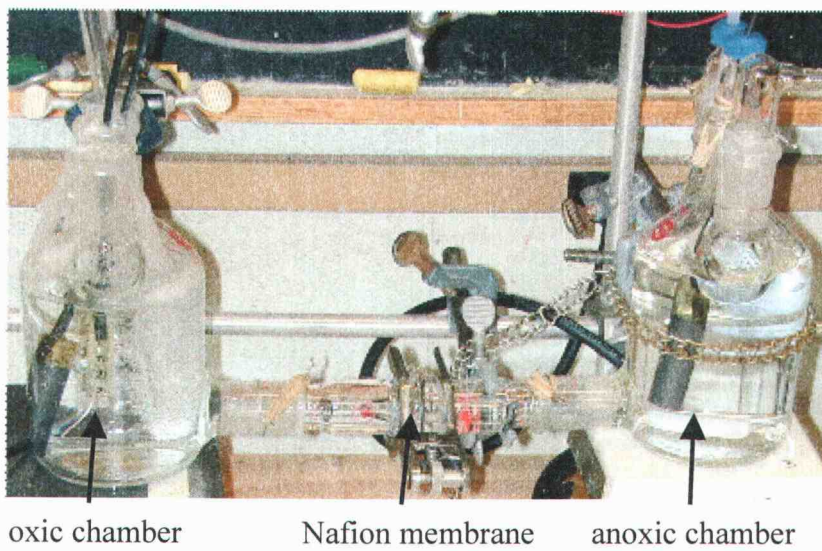
prepared using a Jones reductor: 0.5 N chromic chloride in 0.5 N HCl was reduced through zinc granules previously regenerated with 1 N HCl and stored under N₂ atmosphere. Sulfide concentrations were determined spectrophotometrically following Cline (1969): appropriate concentrations of diamine reagent were allowed to react with ZnS that precipitated in the traps. Absorbance was read at 670 nm after sample dilution. Standards were prepared by dissolution of Na₂S·9H₂O crystals (reagent grade, Fisher scientific, Fair Lawn, NJ) in de-oxygenated DI-water and treated in the same way as ZnS precipitates.

- Organic carbon and total nitrogen: Organic carbon and total nitrogen contents in sediment were determined with a CHN analyzer coupled with gas chromatography (VERARDO et al., 1990). Duplicate subsamples of sediment were dry and then pulverized into a fine powder to homogenize each sample. Silver capsules were filled with 7 to 10 mg dry sediment, humidified with 20 µL de-ionized water and exposed to acid fumes (concentrated HCl) for 24 hours in order to eliminate inorganic carbon (mainly carbonate). Then the treated samples were rolled into tin capsules. Samples introduced in the CHN analyzer are degraded by oxygen combustion at 1000°C; the presence of tin increases the temperature in the column up to 1500°C. Generated gases are successively trapped by Cu (O₂ reduction) and by magnesium perchlorate (water absorbent). Remaining gases (N₂ and CO₂) are separated by gas chromatography and detected by thermo-conductivity. Carbon and nitrogen were standardized with cystine, which contains 29.99 w% C and 11.66 w% N.

II.6. Laboratory simulations of the marine fuel cell under sterile conditions.

Device: A two-chamber fuel cell was constructed with 3-neck aspirator bottles of 500 mL (Labglass, Buena, NJ), joined by 2 glass adapters inserted in the aspirator neck and connected by a pinch clamp (figure 4). Cells were separated by a cation-selective membrane (Nafion117, Aldrich Chemical Company, Milwaukee, WI). Reagents and glassware were sterilized by autoclaving 20 min at 120°C. Tubing used for gas flow was rinsed with denatured ethyl alcohol. Each chamber was filled with 550 mL of sterile 0.7 M NaCl and bubbled for 30 min, the oxic chamber with air and the

Figure 4: Picture of the two chambers used for the laboratory simulations.



anoxic chamber with N_2 ; gas was passed through a 0.3 μm -pore-size HEPA-VENT disposal filter (Whatman). The cathode chamber was opened to the atmosphere, while the top of the anode chamber was sealed with glass adapters. In each cell, electrodes were inserted through the central neck; the two others were used to hold the gas bubbler and as a sampling port. Electrodes were 46 mm to 49 mm long and 12.5 mm diameter graphite rods (LG graphite grade 10, Graphite Engineering and Sales, Greenville, MI). Each electrode surface was cleaned with sand paper and autoclaved prior to use. Cathodes were soaked for one week in sterile 0.7 M NaCl to precondition the surface. The oxic chamber also contained a bare-wire Ag/AgCl reference electrode. During the experiment, the cathodic cell was kept aerated. However only the headspace of the anode chamber was continuously flushed with N_2 to limit sulfide degassing; the solution was homogenized with a magnetic stirrer. The anoxic chamber was enriched with two successive 5 mL additions of 100 mM sterile Na_2S . In order to maintain the pressure equilibrium between the 2 chambers, 5 mL of sterile de-ionized water was added to the oxic chamber at the same time of each sulfide addition to the anode chamber. Data was recorded by a logging multimeter (Agilent 34970A; Agilent Technologies, Palo Alto, CA).

Electrochemical measurements: Two experiments were run. In the first, whole-cell potential (cathode vs. anode) and half-cell potential (anode vs. reference electrode) were monitored at open circuit. In the second, a whole cell potential of 0.3 V was imposed after the first sulfide addition using a potentiostat Model DLK60 (Analytical Instrument System Inc, Flemington, NJ). Variations in whole-cell potential, half-cell potential and current were recorded. Each experiment was run for 6 days, with sulfide injection every 3 days.

Analyses: Samples were drawn regularly from the anode chamber for HS^- analyses. Aliquots were immediately transferred into diamine and analyzed spectrophotometrically (CLINE, 1969) after appropriate dilution. At the end of each experiment, pieces of graphite from the anode were cut and immediately embedded in epoxy (see below) for later surface analysis.

II.7. Electron microprobe analyses and SEM images

Anode surfaces from the laboratory simulations and the Yaquina Bay experiment were analyzed by electron microprobe. These graphite sections were compared to a piece of graphite coming from an unused electrode. Electrode pieces were mounted transversally and analyses were performed across and along the outer edge of the electrode. Graphite samples from the Oregon experiment were first dried for 20 min in the oven at 40°C and then mounted in standard epoxy resin (epo-kwick kit, Buehler LTD, Lake Bluff, IL). Samples from the two-chamber experiment were directly embedded without drying in hydrophilic epoxy (Nanoplast FB-101 embedding resin kits, SPI supplies, West Chester, PA) using a ratio of 30 g of melamine and 0.45 g of hardener. The epoxy was allowed to harden at 40°C in an oven containing open containers of silica gel desiccant for a week. Sample polishing was carried out with progressively finer grades of abrasive, starting with sand paper and finishing with very fine alumina and diamond paste (METADI II Diamond Paste, Buehler LTD, Lake Bluff, IL). To avoid surface charging each polished sample was carbon coated (carbon has minimal effects on the X-ray spectrum). Electron microprobe analyses were performed with an accelerating potential of 15.1 kV, a beam current of either 49.65 nA or 30.03 nA and a beam size of 5 μm . The electron microprobe was equipped with four wavelength-dispersive spectrometers (for different wavelength ranges), with proportional gas (argon) counter detectors. Thirteen elements were detected and quantified: C, O, N, Na, Al, Si, P, S, Cl, K, Ca, Mn, and Fe. Each element detection was referred to a crystal and a counting time was assigned, with background counting times equal to half peak counting times. Prior to sample analysis, each element was calibrated with a reference standard. The ZAF correction was applied in the conversion of X-ray intensities to concentration. This factor eliminates the matrix effects by taking into account the atomic number (Z), the X-ray absorption (A) and the secondary fluorescence (F) of the elements. The uncertainty on the measurements due to random errors associated with the generation and detection of X-rays were evaluated using counting statistics. A scanning electron microscope (SEM) was used in association with the electron microprobe. It served to select areas for elemental analysis. It was also a means for focusing the electron beam on the sample, which corrects the angle of the

emitted X-ray. Images were recorded in the backscattered electron mode which reveals differences in the composition since backscatter is a function of elemental mass. X-ray mapping was also performed: electron microprobe spectrometers were selected for a specific element, while the SEM scanned the sample surface. This technique gives qualitative information about the spatial distribution of the element based on the intensity of its characteristic X-ray line.

III. RESULTS

III.1. The fuel cell

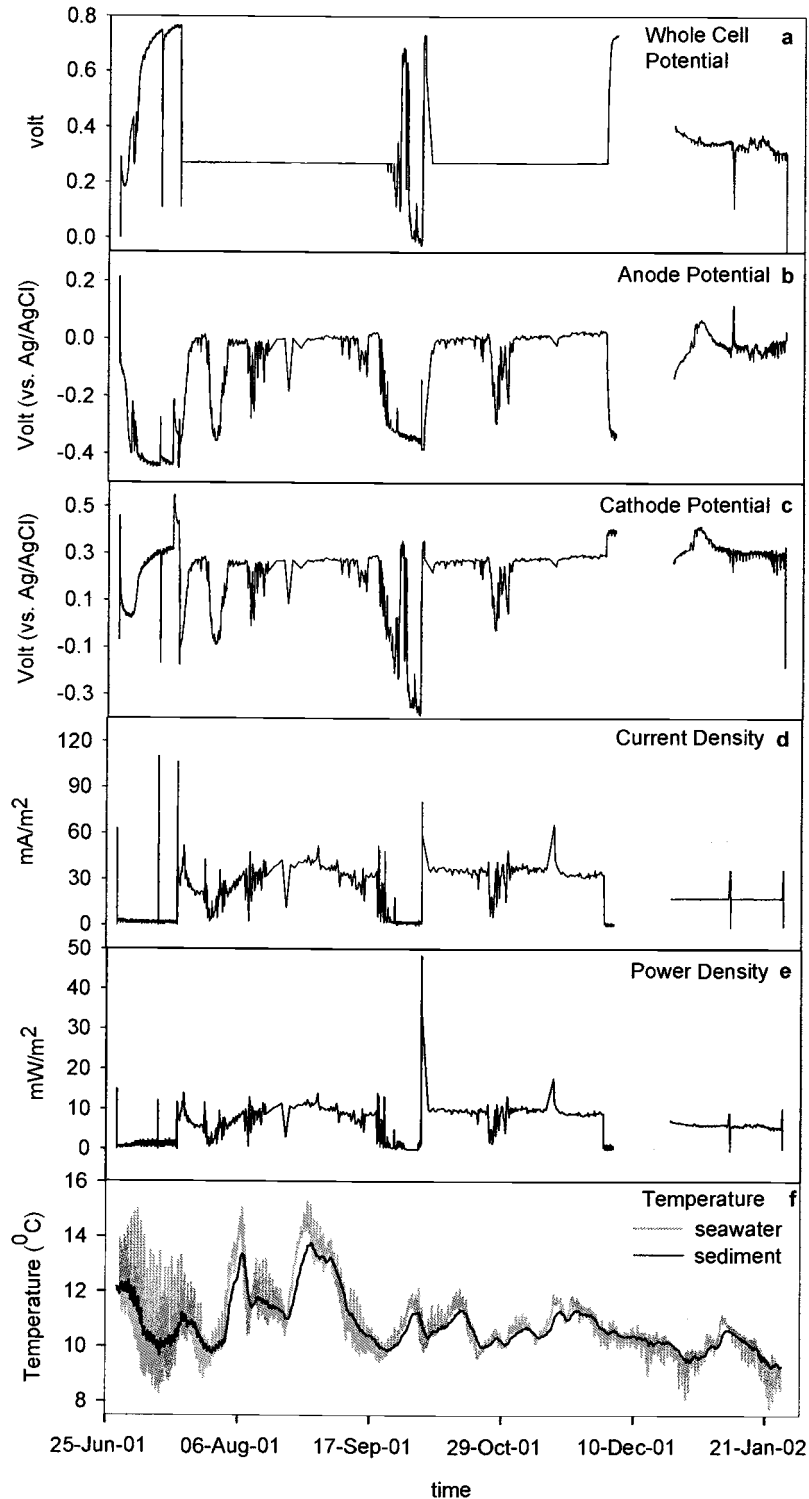
The fuel cell experiments conducted in Yaquina Bay (Oregon) and in the Tuckerton salt marsh (New Jersey) were designed initially to evaluate the electrochemical behavior of cells when operating under natural conditions rather than in the laboratory. Of the two, the Oregon experiment was the most carefully documented and thoroughly sampled post-recovery. For this reason a complete history of its electricity production is reported. This record will be used subsequently to infer the total moles of electrons passed through the Yaquina Bay fuel cell anode.

The Yaquina Bay experiment was deployed on June 28th 2001 and run for approximately seven months. Variations of whole-cell (WC) potential (cathode vs. anode), anode half-cell (AHC) potential (anode vs. reference electrode), cathode half-cell (CHC) potential (cathode vs. reference electrode), current density, power density (WC x current density) and temperature are displayed in figure 5.

The experiment was started with the cell at open circuit, and it took 13 days for the system to reach a near equilibrium potential (WC = 0.75 V). This state corresponded to CHC and AHC potentials of 0.3 V and -0.45 V (vs. Ag/AgCl), respectively. Two rapid tests of cell performance, called “polarizations” (JONES, 1996), were applied on Jul. 11th and Jul. 17th: WC potential was decreased from 0.75 V by 0.01 V every 3 min. The fuel cell responded instantly and for both polarizations the current density increased to a maximum of 110 mA/m² when the WC potential reached a minimum of 0.11 V. The system recovered in between the two polarizations and reached again the open circuit value (0.75 V) after 6 days.

During the next 4.5 months (from Jul. 17th to Nov. 30th), the fuel cell was set at a constant potential of 0.27 V in order to poise the system to draw near maximum power and then to evaluate relative shifts in half-cell potentials and current production as a function of environmental variables. This mode of operation is sometimes called two-electrode amperometry (BARD and FAULKNER, 2001). Under the regulated load, CHC and AHC voltages were variable. Cathode and anode potentials shifted by equal amounts in order to maintain a constant potential difference between the two electrodes.

Figure 5: Whole cell potential (a), anode potential (b), cathode potential (c), current density (d), power density (whole-cell potential x current density) (e) and temperature (f) recorded during the seven-month experiment in the Yaquina Bay Estuary. The cathode half-cell potential and the power density were calculated from the measured parameters (whole cell potential, anode potential and current). Current and power values were normalized to the total anode surface area (0.567 m^2).



They stabilized most often around 0.27 V (figure 5c) and 0 V (figure 5b) (vs. Ag/AgCl), respectively. Variations in current also followed these half-cell potential oscillations: a voltage drop coincided with a decrease in current. But generally current increased during the first 6 weeks to reach a maximum value of 40 mA/m². The combination of constant potential and variable current resulted in an average power density of 11 mW/m² (figure 5e).

An interruption in power generation occurred between Sept. 22nd and Oct. 3rd. During this period, the deployment site of the fuel cell was subject to high inputs of sedimentary material mixed with macroalgae which buried the cathode and eliminated the potential difference existing between cathode and anode environments. Consequently, the fuel cell was no longer able to sustain the imposed WC value of 0.27 V and current flow ceased. Twice (Sep. 25th and Oct. 2nd) divers cleaned off the cathode and WC voltage rebounded to open circuit values (0.70V - 0.73 V). The second time the cathode was cleared, about 10 cm of new sediment was also removed from under the electrode. Then the system was again set to draw current at a fixed cell potential of 0.27 V.

The cell turned off on Nov. 30th due to an instrumentation problem with the Scribner 870, ending the part of the experiment when the WC potential was held at 0.27 V. With no current flow, again the fuel cell voltage rose to 0.73 V (open circuit value) while the anode potential fell to -0.34 V. On Dec. 10th the Scribner 870 instrument was recovered from the seafloor leaving the electrodes in place. After several unsuccessful attempts to repair the deployable instrument, a second 870 programmable load was located within the dockhouse above the experimental site and on Dec. 21st connected to the fuel cell through 30 m-long cables. The long cables increased the noise in current and voltage data, and added resistance (~ 0.5 ohm) that caused a voltage drop of a few mV. However, direct monitoring and control of current flowing between the fuel cell electrodes were renewed.

A constant current value of 10 mA was then imposed to the fuel cell between Dec. 21st and Jan. 25th. During this period the device maintained WC potentials of 0.30 - 0.35 V, with AHC and CHC values of -0.05 - 0.00 V and 0.25 - 0.30 V, respectively. Shifts in WC potential were reflected primarily at the anode. The cathode potential was

quite constant, showing only small regular oscillations, dominated by tidal cycles, also amplified by daily changes of light and temperature. Constant current and nearly steady WC voltage produced a power density of about 6 mW/m^2 . The system was able to sustain 10 mA (18 mA/m^2), indicating the sources of reductants in the sediment were sufficient to continuously provide electrons to the anode. In contrast on Jan. 9th the current density was raised to 36 mA/m^2 . This current could only be sustained for 6 hours and decreased the WC potential to 0.10 V , lowering the power density to 3.6 mW/m^2 . Measurements of electrical parameters were ended on Jan. 26th, when the experiment was recovered and the surrounding sediment sampled.

III.2. Sediment geochemistry

Impacts of the anode reactions of the Yaquina Bay and Tuckerton fuel cells on the local sediment geochemistry may be inferred from differences between the depth profiles of porewater and solid-phase constituents of sediments sampled in proximity to the active fuel cell anodes and those from the control sites (figures 6 - 10). Depth profiles are referred to the position of the active anode (left Y axes of figures 6 - 10). In Yaquina Bay, the active anode was located 20 cm below the seafloor/seawater interface (indicated by the right Y axes of figures 6 - 8) at the time of recovery, and the control anode was buried 5 cm shallower. The two additional samples scrapped from the surface of the active anode provided replicate information about the geochemistry corresponding to the color change (figure 3).

The depth profiles of porewater and solid-phase compounds from the Yaquina Bay sediment cores were broadly similar at both active and control sites (figures 6 - 8) and displayed typical overall patterns for this coastal environment (POWELL, 1980). Irregularities in depth distributions such as those seen in between 0 and -15 cm depth in the silicate profiles (figure 6h) were probably consequences of bioturbation and irrigation. As previously indicated, new sediment became trapped beneath the active fuel cell cathode during the experiment. As a consequence, sediments surrounding the energy-harvesting anode were richer in organic carbon and total nitrogen than those at the control site. The organic matter content at the active and control sites, respectively,

Figure 6: Porewater profiles associated with the experiment in Yaquina Bay Estuary. Distributions of dissolved species from along side and above the control graphite electrode and above the anode of the fuel cell are presented. Error bars correspond to plus or minus one standard deviation of duplicate sediment samples from the same interval.

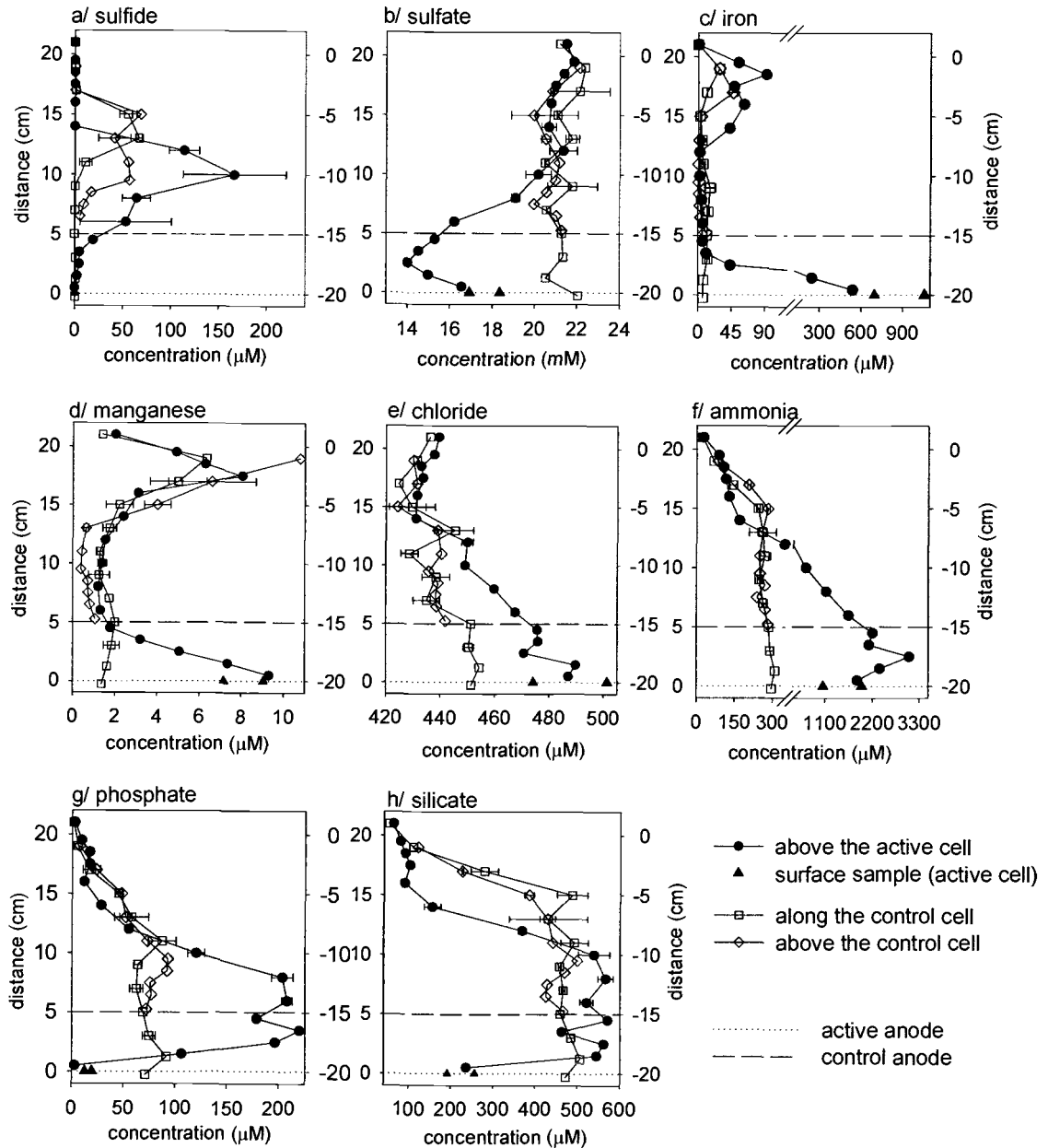
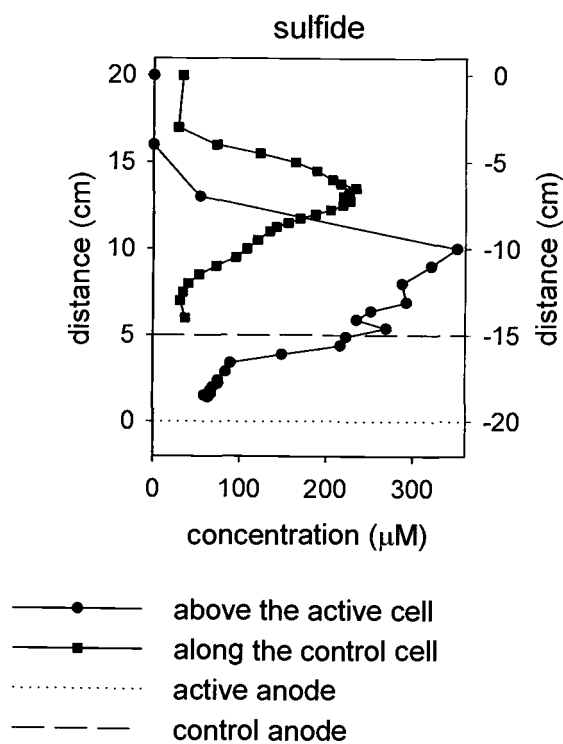


Figure 7: Sulfide profiles of sediment cores from the Yaquina Bay experiment, measured by voltammetry; comparison of the distribution of total dissolved sulfide above anodes of control and active devices.

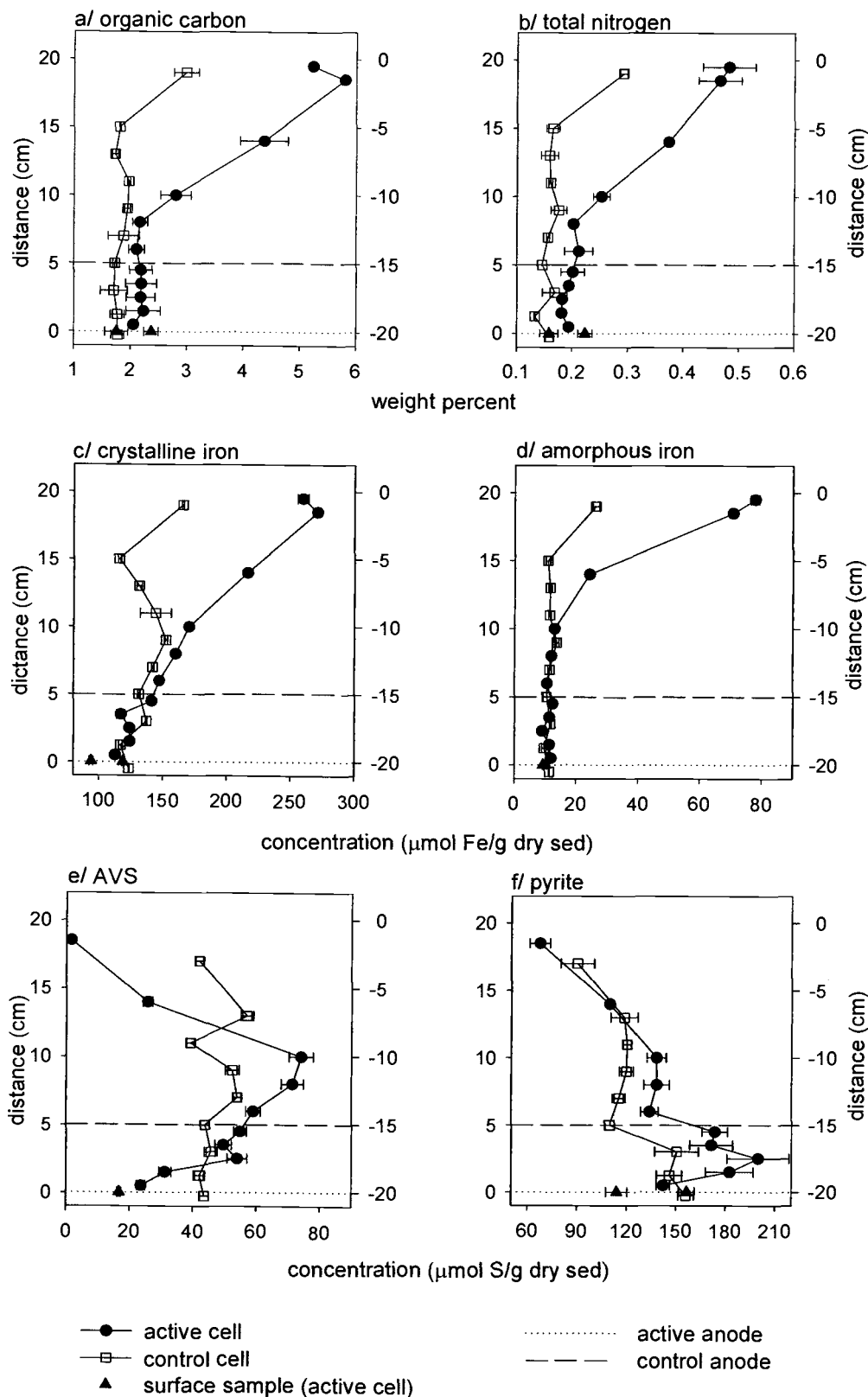


decreased from 5%OC - 0.5%TN and 3%OC - 0.3%TN at the sediment/seawater interface to 2.2%OC - 0.2%TN and 1.7%OC - 0.15%TN at the electrode surfaces (figure 8a - b). The higher amount of organic matter in the sediment surrounding the active cell was accompanied by steeper concentration gradients in many dissolved and solid phase chemical constituents.

At both active and control sites dissolved oxygen was depleted in the first few millimeters of the sediment column (data not shown). Dissolved iron and manganese distributions were characterized by subsurface peaks with respective concentrations of 96 μM and 8 μM at a depth of -3 cm above the active anode (figure 6c - d). Although the iron measurements represent total dissolved Fe, Fe(II) species are assumed to have been the dominant dissolved form of iron because Fe(II) is highly soluble and produced through microbial reductions of solid-phase Fe oxides. The concentration maximum of dissolved iron and manganese indicates the presence of a suboxic zone where organic matter oxidation is associated with the microbial reduction of Fe and Mn oxides. Sulfate concentrations were nearly constant at 20 mM in the Fe/Mn reduction zone and then decreased to 14 mM at the active site (figure 6b). Profiles of sulfate/chloride ratio (data not shown) have patterns similar to sulfate alone due to relatively small downcore variations of chloride concentration (< 10 %). Such sulfate gradients and corresponding increases in ammonia (figure 6f) and phosphate (figure 6g) are characteristic of anoxic marine environments (JØRGENSEN, 1977) where the microbial oxidation of organic matter depends upon sulfate reduction. The lack of a sulfate gradient (figure 6b) and the small increases in ammonia (figure 6f) and phosphate (figure 6g) between -10 and -20 cm depth at the control site suggest that sulfate reduction rates were lower. This pattern is consistent with a lower organic matter input.

Sulfate-reducing bacteria enrich anoxic environments in total dissolved sulfide. Figure 6a shows sulfide maxima (50-150 μM) 8 -10 cm below the seafloor boundary at both active and control sites. Voltammetry measurements in separate cores presented similar patterns (figure 7) but with higher total sulfide concentrations located at a depth of -8 cm and -10 cm for the control and the active sites, respectively. This may indicate

Figure 8: Solid phase profiles associated with the experiment in Yaquina Bay Estuary. In comparison are of the distributions of solid-phase species from along side the control graphite electrode and above the anode of the fuel cell. Error bars correspond to plus or minus one standard deviation of samples analyzed in triplicate.



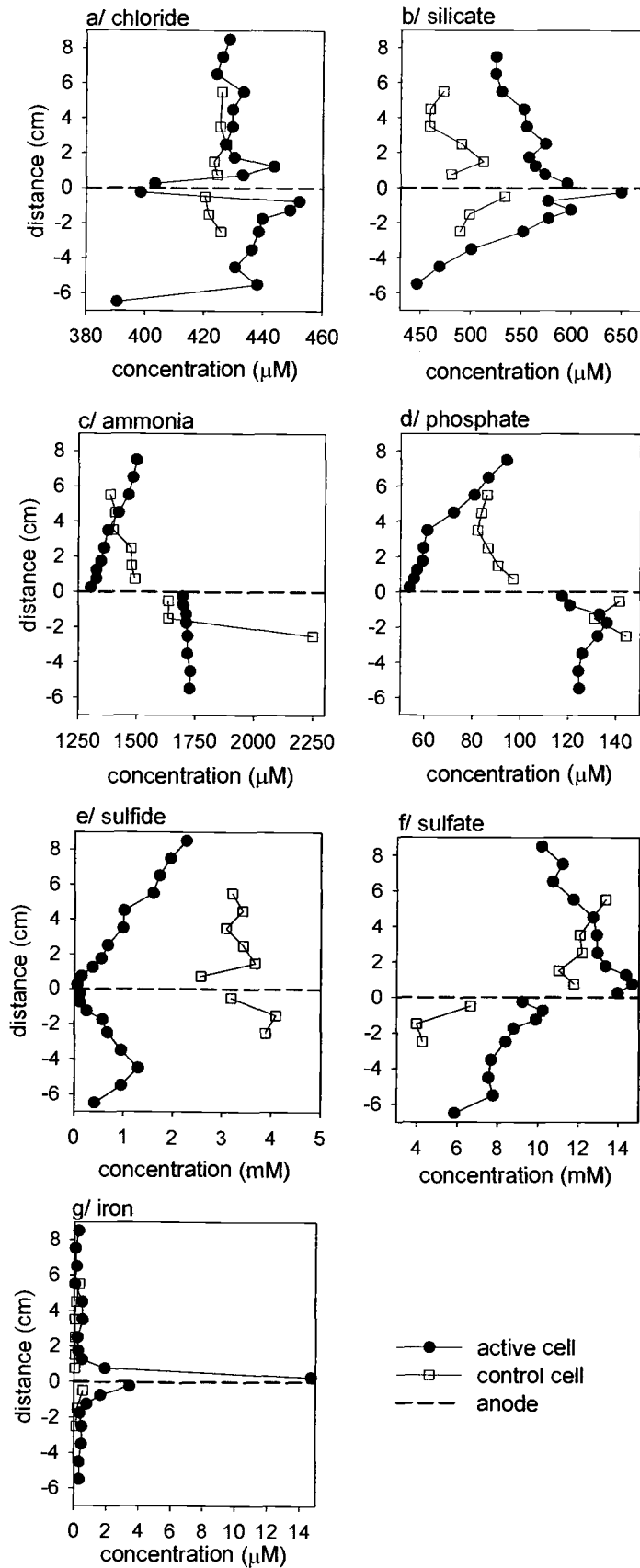
that sulfide was not homogeneously distributed in the sediment column, or that the microelectrode was sensitive to additional colloidal sulfide species (LUTHER III et al., 2001; ROZAN et al., 2000).

Dissolved sulfide concentrations can be regulated in coastal sediments by reactions with iron to form iron-sulfide minerals (BERNER, 1970; BERNER, 1984; BERNER, 1985; GOLDHABER and KAPLAN, 1975; LIN et al., 2002; LIN and MORSE, 1991; WANG and MORSE, 1996). The first product to precipitate is FeS that can be detected as AVS. AVS concentrations were highest (80 $\mu\text{mol S/g}$ dry sediment) at a depth of -10 cm which also corresponded to the depth where the dissolved sulfide concentration was maximal (figure 8e). Beneath this peak, the AVS content decreased gradually to 20 $\mu\text{mol S/g}$ dry sediment. This trend is consistent with pyritization, i.e. the transformation of metastable iron sulfide compounds to FeS_2 , which is a more stable mineral thermodynamically under sedimentary conditions (BERNER, 1964). Pyrite increased generally with depth from 60 $\mu\text{mol S/g}$ dry sediment to 150 - 200 $\mu\text{mol S/g}$ dry sediment (figure 8f).

Figure 8c and 8d show a significant loss of amorphous Fe (20 - 70 $\mu\text{mol Fe/g}$ dry sediment) and crystalline Fe (50 - 100 $\mu\text{mol Fe/g}$ dry sediment) in the upper 10 cm of the sediment column. This decline of iron oxides probably reflects the microbial reduction of Fe(III) minerals producing dissolved Fe^{2+} (figure 6c), or reactions of Fe(III) minerals with HS^- leading to the formation of AVS (figure 8e) and pyrite (figure 8f).

The bottom part of the sediment cores (up to 3 cm above the active anode) showed significant shifts in most of the profile trends at the active site only. Figure 6a - c indicates sulfide depletion and large enrichments of dissolved iron (up to 1 mM) and sulfate (4 - 5 mM) in porewaters approaching the active anode but not near the control anode. Porewater profiles also showed an increase of 8 - 9 μM in manganese (figure 6d). These patterns suggest that these redox species played a significant role in the electron transfer to the anode, with sulfide as a source of electrons and Fe^{2+} , SO_4^{2-} and Mn^{2+} as by-products of anodic reactions. Nutrient profiles also showed differences between active and control sites near the embedded electrode: ammonia, phosphate and silicate decreased by 1 mM (figure 6f), 220 μM (figure 6g) and 400 μM (figure 6h),

Figure 9: Porewater profiles associated with the experiment in the Tuckerton NJ salt marsh. In comparison are the distributions of dissolved species above and below the control graphite electrode and the anode of the fuel cell.



respectively, toward the anode under the influence of the fuel cell, whereas profiles above the control anode did not indicate concentration changes with depth. The loss of PO_4^{3-} and H_4SiO_4 may be in part an artifact of the sampling procedure: the high Fe content in these samples (figure 6c) was oxidized and precipitated (yellow and cloudy appearance) before nutrient analysis. Phosphate and silicate tend to adsorb onto iron oxides, reducing the concentration in the dissolved phase (POKROVSKI et al., 2003; ROZAN et al., 2002).

The fuel cell mechanism did not seem to have a measurable effect on the bulk organic matter (figure 8a - b). Organic carbon and total nitrogen distributions were similar above the control and active anodes, with respective concentrations of 1.8 - 2.3% OC and 0.15 - 0.22% TN below 12 cm from the sediment/seawater interface. Amorphous and crystalline iron oxides also were not affected by the presence of the fuel cell (figure 8c - d). Such profiles indicate that Fe(III) was not used as a major electron acceptor by bacteria associated with the active anode and so was not the source of the rich iron concentrations in the porewater from near the surface of the active anode (figure 6c). Other solid phases containing iron are sulfide minerals. Pyrite and AVS decreased by 100 $\mu\text{mol S/g}$ dry sediment and by 40 $\mu\text{mol S/g}$ dry sediment, respectively, toward the anode of the active cell, whereas profiles from the control site indicated no losses of iron sulfides (figure 8e - f).

In contrast to the Yaquina Bay study, the enclosed device and sediments used in the Tuckerton experiment experienced limited exchanges with the marine environment. Despite this difference in the experimental design, distribution patterns of redox species (HS^- , SO_4^{2-} and Fe^{2+}) showed similar alterations near the active anode during both experiments. Figure 9e - g indicates sulfide depletion and production of sulfate (4 mM) and dissolved iron (14 μM) approaching the active anode. The salt marsh sediment was initially richer in sulfide (3 - 4 mM) than the estuarine sediment. The control profiles had invariant depth distributions for these constituents, suggesting that changes observed at the active site were a consequence of the energy-harvesting mechanism. Nutrient profiles also showed variations of concentration at the active anode surface that were greater than near the control electrode: NH_3 and PO_4^{3-} decreased by 200 μM

Figure 10: Solid phase profiles associated with the experiment in the Tuckerton NJ salt marsh. In comparison are distributions of solid-phase constituents from above the control graphite electrode and the anode of the fuel cell. Samples were analyzed in triplicate and error bars correspond to plus or minus one standard deviation.

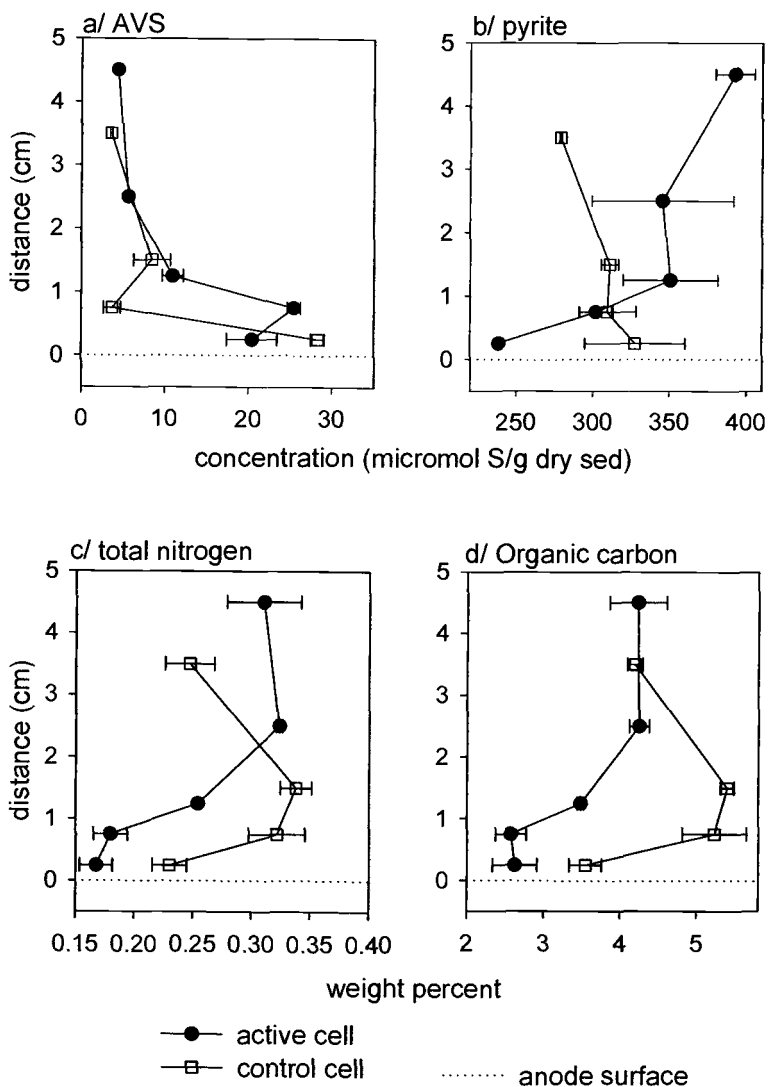


(figure 9c) and 50 μM (figure 9d), respectively. Silicate had an opposite trend compared to the estuarine profiles: concentration increased at the anode surface (figure 9b). This difference may confirm the hypothesis of silicate adsorption or coprecipitation with iron after porewaters from the Oregon experiment were extracted, because the iron content in the salt marsh sediment was about 100 times less (figures 6c and 9g). Top and bottom cores also showed concentration offsets at the electrode surfaces. This is thought to be a consequence of the sampling procedure: top and bottom cores were not aligned with the anode in between. Instead they were taken from different regions of the 167 L container. Some areas may have been influenced by greater porewater exchange through the screen-covered openings in the containers. These dilutions effects may explain the minima in chloride (figure 9a).

Solid sulfides presented similar patterns to the Yaquina Bay profiles. AVS and pyrite concentrations decreased by 10 and 100 $\mu\text{mol S/g}$ dry sediment, respectively, only near the active anode (figure 10a - b). Distributions of organic carbon and total nitrogen content in the sediment solid phases were irregular at both the active and control sites, showing opposite trends to those observed for the Oregon experiment. It is unknown how much these profiles were determined by the initial packing of sediments around the anodes when the devices were deployed.

In summary, sediment analyses at both sites indicated that compounds related to sulfur chemistry were strongly affected by the fuel cell activity, with a loss of reduced sulfur species (HS^- , FeS , FeS_2) and production of oxidized forms (SO_4^{2-}). Nutrient and dissolved iron concentrations also varied under the influence of the fuel cell.

III.3. Anode surfaces

Backscattered electron (BSE) images of sections of the Yaquina Bay electrodes revealed some similar compositional features at both control and active anode surfaces (figure 11). Both graphite sections were covered with a 200 - 250 μm thick layer. Microprobe profiles indicated high nitrogen content in this surface coating (figure 13a), confirming the presence of a biofilm (table 1). Specific areas in the biofilm produced a high amount of backscatter indicating the presence of mineral grains (Si-rich). Low density zones were more abundant in the deposit layer covering the energy-harvesting

Figure 11: BSE images of surface cross-sections of the graphite electrodes that were buried in Yaquina Bay. These images allow the comparison the fuel cell and the control cell

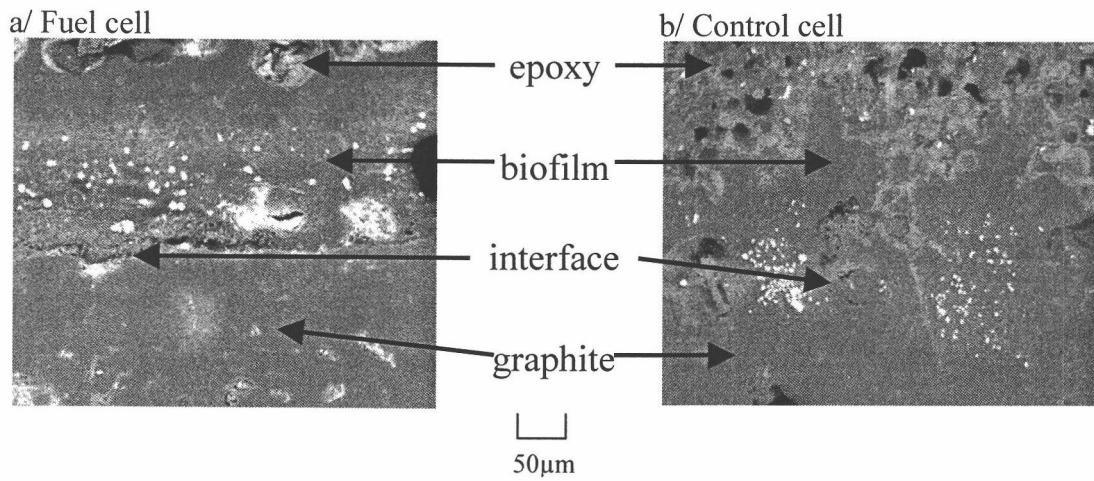
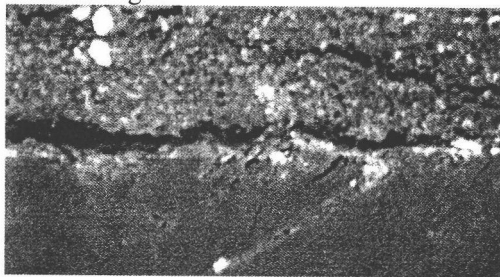
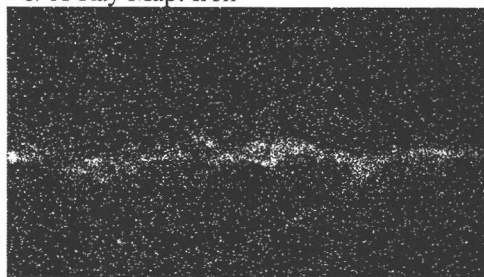


Figure 12: Spatial elemental analysis by X-ray mapping of the distribution of iron (b), oxygen (c) and sulfur (d) on a cross-section of the active anode from the Yaquina Bay experiment. The BSE image (a) refers the elemental maps to the different phases present at the electrode surface. Accumulation of white dots indicates higher elemental concentration.

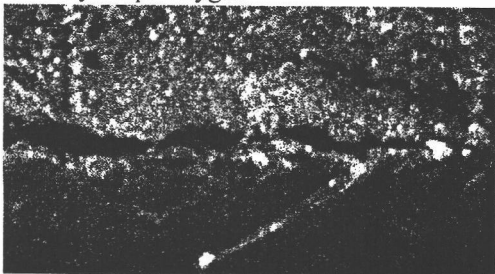
a/ BSE images



b/ X-Ray Map: Iron



c/ X-ray Map: Oxygen



d/ X-ray Map: Sulfur



60µm

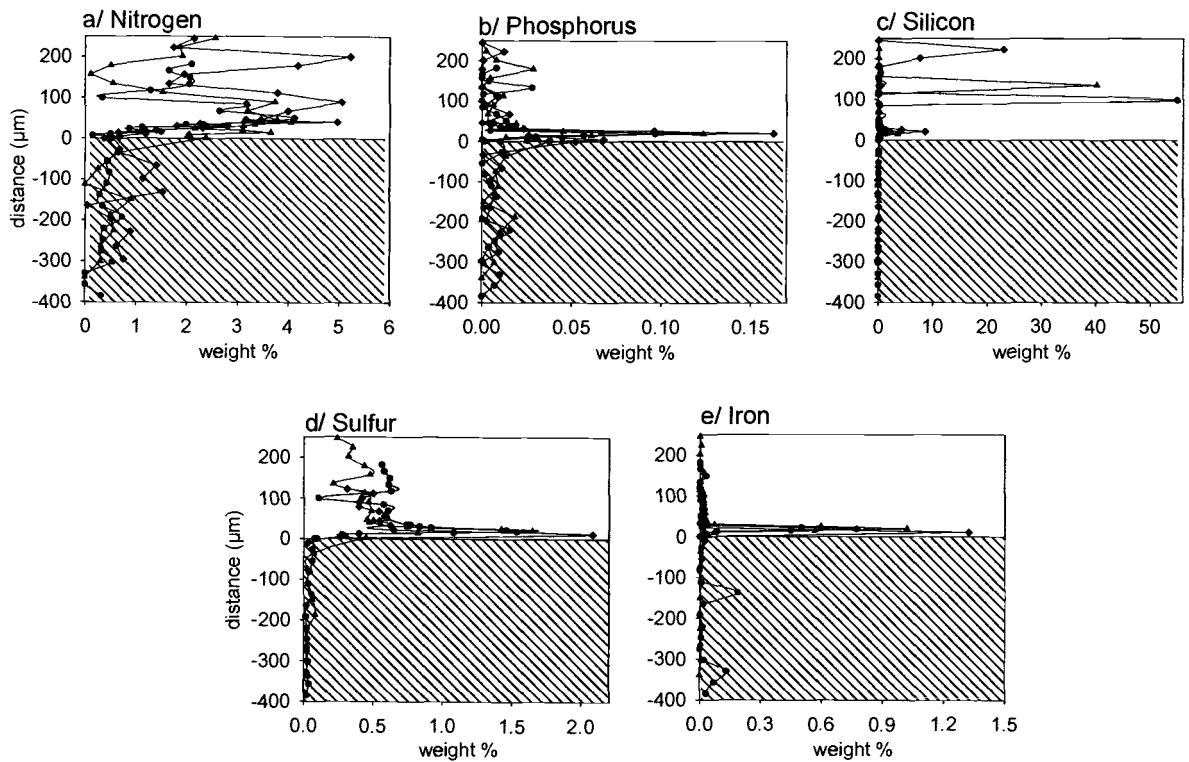
anode than the control anode, and these spots were N-rich. A gap present at the biofilm-graphite surface may have been caused by the stresses of sample polishing.

The main difference between the active and control cell samples was located at the graphite/biofilm interface: a separate layer between the two phases is clearly apparent in images of the active anode (figure 11a), but hardly visible in images of the control anode (figure 11b). Elemental maps in figure 12 indicate an accumulation of iron and sulfur at the biofilm-electrode boundary and a high S content in the deposit layer.

Spatial differences in concentration were quantified for several elements by electron microprobe. The elemental composition of the surface of the control anode was similar to the reference graphite sample (data not shown). Figure 13 shows elemental profiles across the anode surface of the active fuel cell. Nitrogen was quite homogeneously distributed in the biofilm, with a content between 2 and 5 wt % (figure 13a), except in areas of high Si concentration. Silicon abundance approached zero percent in the biofilm, with concentration peaks between 20 and 55 wt % randomly distributed in the deposit layer (figure 13c). This pattern was a consequence of the presence of mineral grains. However all Si profiles showed a similar peak reaching 10 wt% 10 - 20 μm above graphite at the interface between the anode surface and the biofilm (figure 13c). This zone also corresponded to an increase in iron and sulfur. These elements respectively reached 1.0 - 1.3 wt% (figure 13e) and 1.6 - 2.0 wt% (figure 13d). The biofilm also stored a significant amount of sulfur (between 1.0 and 1.5 wt %) but was not enriched in iron (less than 0.1%). These results are consistent with the information obtained by X-ray mapping (figure 12 b and d). Phosphorus profiles showed a distribution pattern similar to Fe, with low content (0.02 - 0.04 wt%) in the deposit layer and an increase of concentration to 0.16 wt% at the graphite surface (figure 13b), where iron deposition was greater. Associations of P in the solid phase are often controlled by adsorption to iron precipitates (ROZAN et al., 2002). Elemental mapping showed oxygen at the electrode surface (figure 12c), suggesting that iron may be present as Fe oxides.

Elemental distributions were also measured along the anode surface. Figure 14a and 14b indicate deposition of sulfur and iron on the active anode but not on the

Figure 13: Electron microprobe profiles across the interface of the graphite anode deployed in the Yaquina Bay Estuary (Oregon). 0 μm refers to the electrode surface; streaked area (with negative distance) represents the graphite material; positive distance numbers are located in the biofilm.



control anode. The control electrode exhibited contents of these elements similar to the reference sample of unused graphite. Iron and sulfur were respectively 400 times and 20 times more abundant at the electrode surface of the active fuel cell. These measurements confirmed the local enrichment of iron and sulfur at the electrode surface that was qualitatively shown by X-ray mapping (figure 12b - d). The precipitation of iron at the anode surface also seems associated with sulfur: Fe/S ratios varied linearly ($R^2=0.89$) with iron content (in Atomic %) (figure 15). This finding is consistent with both elements becoming mobilized by the oxidation of iron sulfide minerals (figures 8e, 8f, 10a, and 10b) at the fuel cell anode (developed further in the discussion section).

III.4. Laboratory simulations

Fuel cell experiments were run under simplified laboratory conditions to verify the role of sulfide as electron donor and to determine its effect on the electrode surface. The control experiment was monitored at open circuit (no current), while a steady whole-cell potential of 0.3 V was imposed during a second experiment. These conditions were chosen to be similar to the field experiments in order to compare the results between the two sets of data.

Figure 16a shows the anode potentials (vs. Ag/AgCl), and figure 16b shows the current density measured when the cell was held at 0.3V. The potentials decreased rapidly when sulfide was added at the beginning of both experiments. The AHC voltage of the control experiment never fully stabilized: it slowly decreased to attain -0.52 V (vs. Ag/AgCl) after 6 days. The corresponding WC potential was 0.75 V. This is close to the open circuit value observed in many natural marine environments (figure 5). In contrast, in response to the imposed WC value, the anode potential during the second experiment was relatively steady at a value of -0.22 to -0.25 V (vs. Ag/AgCl). The second addition of sulfide after 72 hours caused the anode potentials to shift by -0.02V in both experimental runs (figure 16a). Before this injection of HS^- , the control and active chambers contained 0.83 mM and 0.79 mM, respectively and the second sulfide addition raised these concentrations to 1.52 mM and 1.56 mM. The small difference in concentration between both experiments was a consequence of the subsampling that altered the quantity of medium present in the chambers. The curve describing the

Figure 14: Sulfur (a) and iron (b) transects along the interface of the graphite anode deployed in the Yaquina Bay Estuary (Oregon), compared to the reference sample (unused graphite). (note log scale)

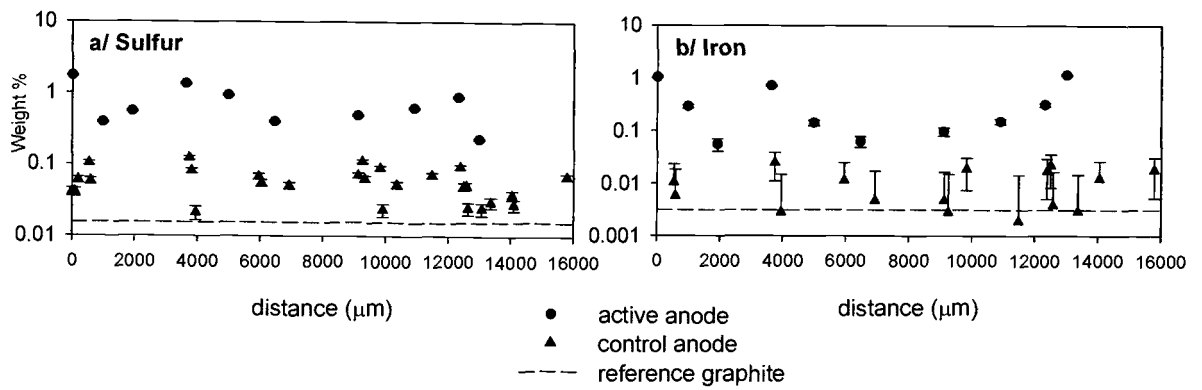
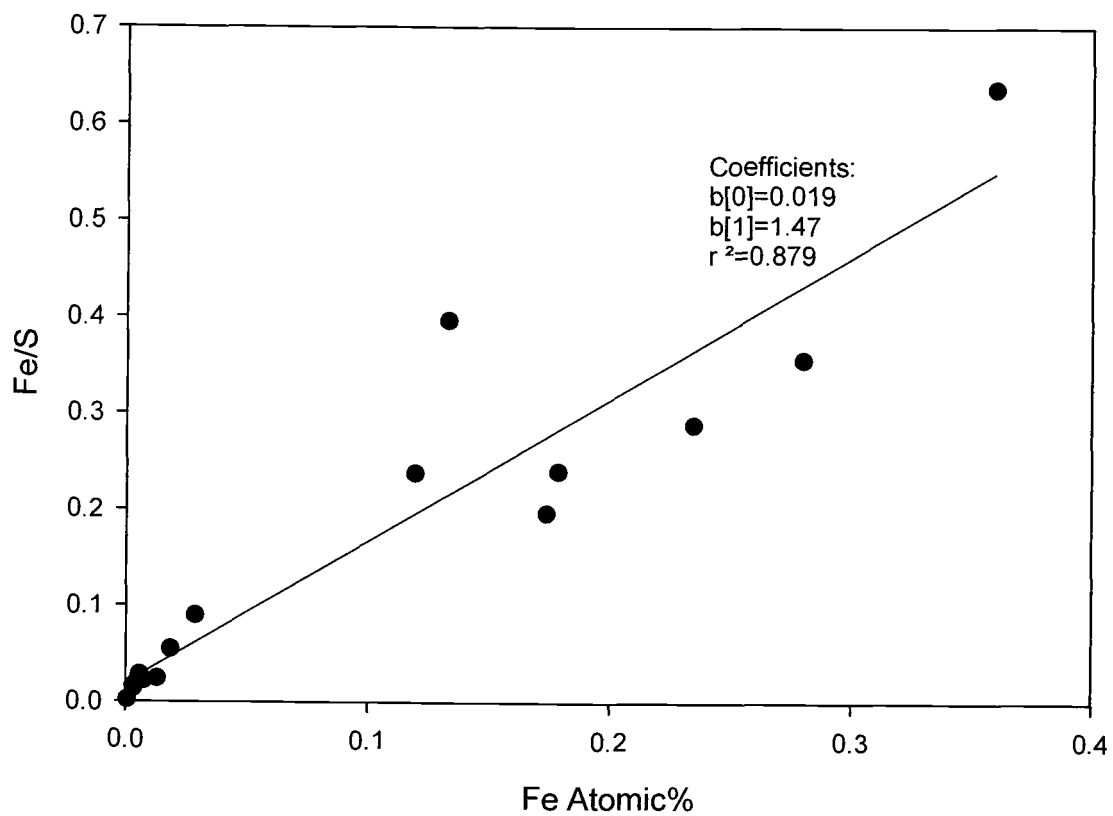


Figure 15: Fe/S atomic ratio as function of the iron content at the interface between graphite and biofilm for the fuel cell anode.



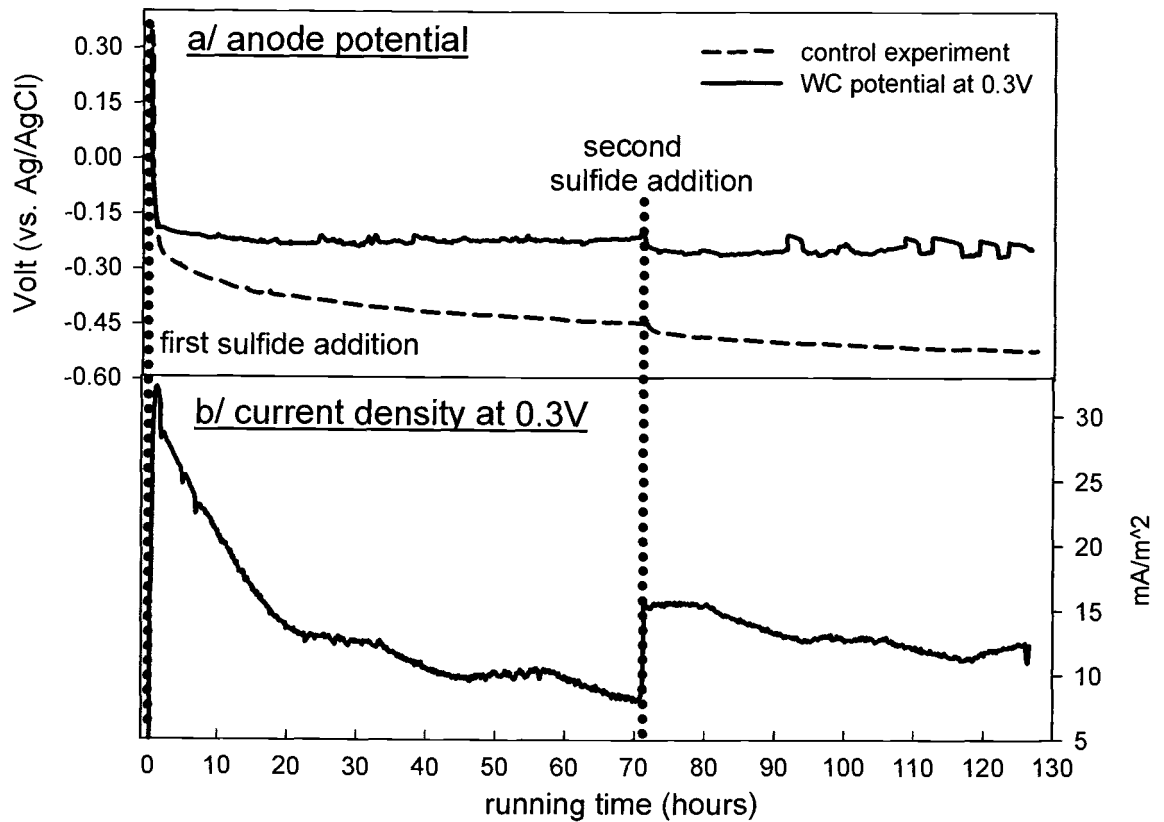
current production (figure 16b) once the potential difference was imposed started with a spike of current (32 mA/m^2) that decreased exponentially at first and then at a slower rate. The second sulfide addition did not generate another spike of current, only an increase from 8 mA/m^2 to 15.5 mA/m^2 . The system also exhibited small diurnal variations with steady currents during the day and small decreases at night. At the end of the control and energy-harvesting experiments, sulfide concentrations were 1.36 mM and 1.33 mM , respectively, representing sulfide losses of 10.5% and 14.5%.

These losses may be compared to the electrochemical oxidation rate indicated in the current producing system. Current was integrated over time and converted to moles of electrons. In total $130 \text{ } \mu\text{moles}$ of electrons were exchanged during the experiment. Assuming the oxidation of sulfide to elemental sulfur transfers 2 electrons per mol of HS^- (ATEYA and ALKHARAFI, 2002b; ATEYA et al., 2003), $65 \text{ } \mu\text{moles}$ of sulfide were oxidized. This represented only 4% of the total amount of sulfide present in the system suggesting that the total exchange of electrons was limited by electrode area and electrode kinetics. Previous studies have had similar findings (ATEYA and ALKHARAFI, 2002b). Total sulfide losses were the result of degassing in addition to chemical oxidation.

Pieces of graphite anode were immediately embedded in hydrophilic epoxy at the end of each experiment for surface analyses. It should be noted the epoxy used was different than what was applied for mounting the Yaquina Bay anode pieces because there was a concern that drying steps may cause artifacts. BSE images (figure 17a and b) indicated a gap of about $50 \text{ } \mu\text{m}$ between the epoxy and the graphite, similar to the field samples. The epoxy covering the graphite also contained the elements of the electrolytes present in the medium (Na^+ , Cl^- , HS^-), probably due to the adsorption and reaction with water at the electrode surface (figure 17c - d). Sulfur accumulated to a greater degree at the epoxy boundary of the control electrode. The active anode showed similar features with elements distributed more homogeneously in the resin.

Important differences between active and control anodes were located at the graphite surface. Small enrichments of sulfur appeared on the graphite surface of the active electrode but not on the control anode (figure 17c - d). The interface between

Figure 16: Variations in the anode potential (vs. Ag/AgCl) (a) and current density (b) during the laboratory simulations, run for 6 days. The control experiment was run at open circuit. When a potential of 0.3V was imposed to the system, the anode half cell voltage shifted as current was produced.



the graphite and the gap on the control electrode was also not visible on X-ray maps indicating no specific chemical deposition. Quantitative electron microprobe data was used to compare the composition of the electrode surface to the underlying graphite (similar transects 50 μm below the surface). The surface of the fuel cell anode presented a relative enrichment of sulfur between 24 and 70 % (figure 18a), while the surface of the control anode had on average only 18 % more S (figure 18b). Transects along the surface of the active anode also indicated that S did not deposit evenly.

This set of laboratory electrochemical cell experiments confirmed that sulfide is electroactive on graphite electrodes connected in the manner of seafloor fuel cells. Sulfur deposition on the graphite surface was also indicated but not to the degree exhibited by the field experiments. These well-stirred simulations also did not have the same transport constraints that may be present in the natural environment, but highlighted kinetic limitations of surface redox reactions.

Figure 17: BSE images (a, b) and spatial distributions of S (c, d) (by X-ray map) on surface cross- sections of anode pieces from the laboratory simulations. Above: control experiment; below: experiment with constant whole cell potential set at 0.3 V. On X-ray maps, whiter areas indicate greater concentration.

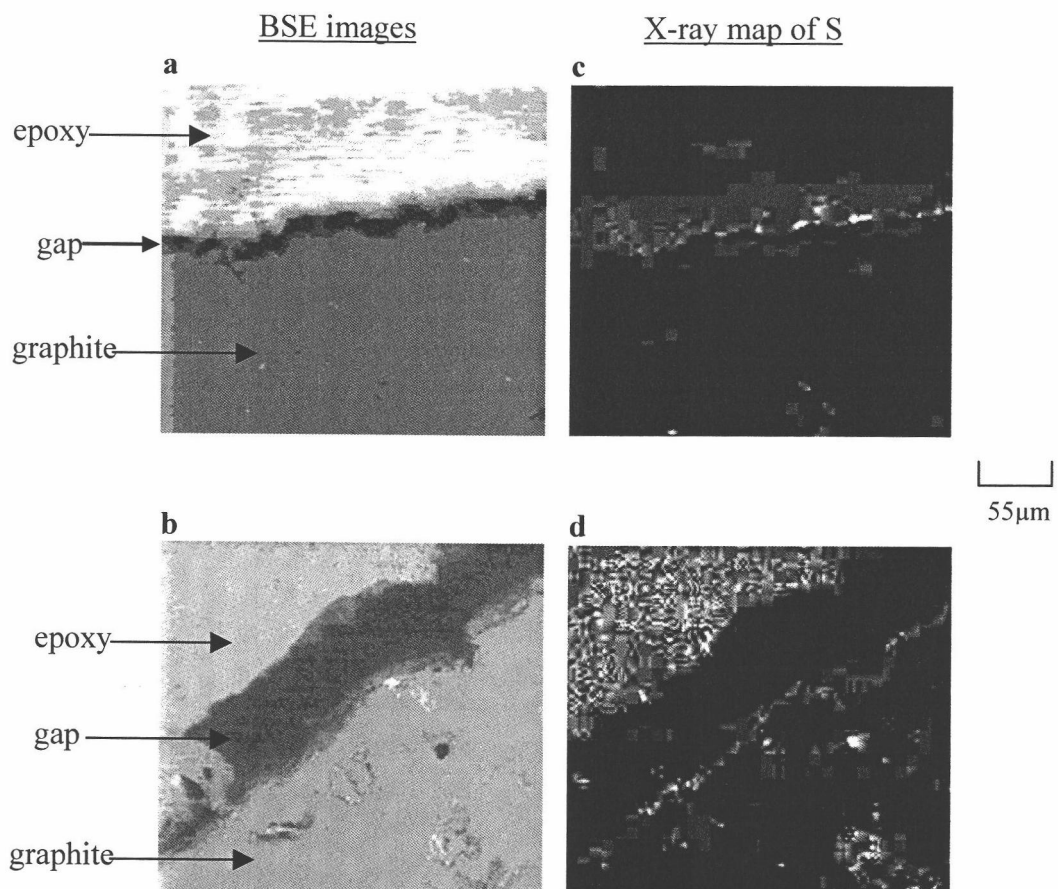
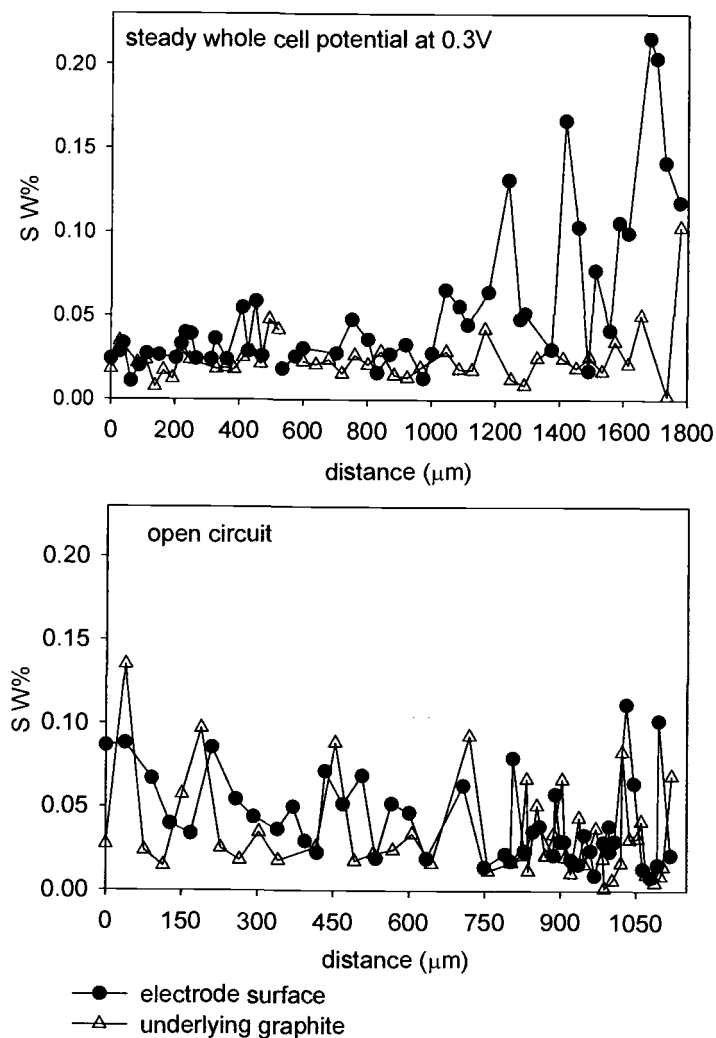


Figure 18: Comparison of sulfur deposition between the open circuit and the energy harvesting experiments; measurements by electron microprobe of sulfur content at the electrode surface and in the graphite material for both experiments.



IV. DISCUSSION

IV.1. Electron transfer to the anode: microbial and/or electrochemical

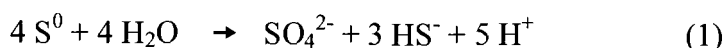
Marine sediments are complex environments where geochemical transformations are often coupled to microbial activity. In the presence of a marine fuel cell these biogeochemical processes, as well as heterogeneous reactions initiated at the electrode surface, may participate to the electricity production. The more favorable reactions are expected to leave their signature. This was the reasoning leading to the sediment and anode investigations in this study.

The analysis of the microbial community covering the active anodes highlighted the selectivity of the fuel cell for certain phylotypes of bacteria (table 1) (HOLMES et al., in press; TENDER et al., 2002). In contrast, no significant enrichments were observed on the control devices. Microorganisms belonging to the δ -Proteobacteria group dominated the gene sequences cloned from the microbial population on the estuary and salt marsh active anodes. The New Jersey anode was specifically colonized by microbes related to *Desulfuromonas acetoxidans* (>95% similarity) (TENDER et al., 2002), a marine representative of the family *Geobacteraceae*.

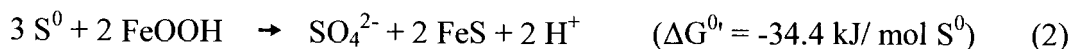
Geobacteraceae are known to use insoluble minerals, such as iron (III) oxides, as electron acceptors. This observation suggests that a graphite electrode may also serve as a terminal electron acceptor for some microbial electron chain reactions if the electrode is poised at a suitable potential. Bond and Lovley (2003) reported the ability of *Geobacter sulfurreducens*, another member of the *Geobacteraceae*, to conserve energy and grow while transporting electrons to a graphite electrode in an anaerobic buffer lacking nutrients. When inoculated with these bacteria, the electrochemical cell produced a maximal power density of 15.5 mW/m² (at 0.47 V) (BOND and LOVLEY, 2003). Similar experiments conducted with a pure culture of *Desulfuromonas acetoxidans*, demonstrated that a current density of 20 - 100 mA/m² could be sustained (BOND et al., 2002). All these results are comparable to the field experiments (figure 5), indicating that bacteria can play an important role in the transfer of electrons to the fuel cell. Further investigations (NEVIN and LOVLEY, 2000) showed that *Geobacteraceae* do not produce electron-shuttling compounds to assist the reduction of Fe(III) minerals.

This suggests that electron transfer to an anode surface may also be facilitated by direct contact of cells.

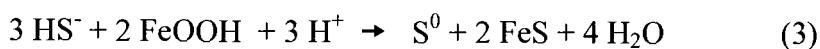
However the absence of *Geobacteraceae* at the surface of the buried electrode of the fuel cell deployed in Yaquina Bay implies that other electron transfer pathways to an anode may have been foremost in this natural system. The dominant microbes on the Oregon electrode corresponded to species of the *Desulfobulbus/Desulfocapsa* genera. These bacteria disproportionate elemental sulfur to sulfate and sulfide, when sulfide concentrations are low (FINSTER et al., 1998; LOVLEY and PHILLIPS, 1994):



This reaction is thermodynamically unfavorable: $\Delta G^0 = +10.2 \text{ kJ/mol } S^0$. Cell growth has been only observed in presence of ferrihydrite (FINSTER et al., 1998; JANSSEN et al., 1996; THAMDRUP et al., 1993):



However a direct participation of iron oxide in the energy metabolism of S^0 -disproportionating bacteria has not yet been proven, as elemental sulfur disproportionation is also carried out in the absence of Fe(III). It seems more likely that ferric iron acts as a sulfide scavenger.



Reaction (3) occurs in reducing sediments between pH 7.0 - 8.5 (PYSIK and SOMMER, 1981).

Since the fuel cell anode is an electron sink, it may play a similar role to that of Fe oxide during sulfur disproportionation, favoring the development of microorganisms that utilize elemental sulfur. This hypothesis was suggested in part by Tender et al. (2002) and is developed further in the next section.

The relatively low levels of total sulfide in Yaquina Bay can be attributed to the high iron concentration in this estuarine sediment (figures 6c, 8c and 8d). It has been shown that in coastal sediment porewater, HS^- is depleted by precipitation with Fe(III) oxides (CANFIELD, 1989a; THAMDRUP and CANFIELD, 1996; THAMDRUP et al., 1994), producing iron sulfide FeS and elemental sulfur S^0 (reaction (3)), with possible further reaction to pyrite FeS_2 (BERNER, 1970):



This is consistent with the increase of AVS (figure 8e) and pyrite (figure 8f) with depth in the Yaquina Bay estuary. The presence of iron enriches the sediment in sulfide minerals, but removes dissolved sulfide except where its production rate is greatest. In contrast, the concentration of dissolved sulfide in the salt marsh porewaters was higher (figure 9e). Figure 6a and figure 9e show depletion of total dissolved sulfide approaching the active anode of the fuel cells. Thus sulfide depletion by the seafloor fuel cell in the two different environments (estuary and salt marsh) suggests that mechanisms involving the oxidation of HS^- participate in the production of energy.

IV.2. Electrochemical oxidation of sulfide

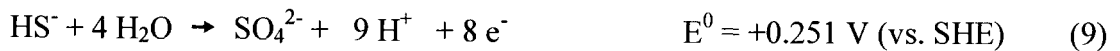
The hypothesis that electricity may be produced by the electrochemical abiotic oxidation of sulfide was tested by simulating a marine fuel cell in the laboratory under sterile conditions. In the presence of HS^- , the two-chamber electrochemical cell reached WC and AHC open circuit values (figure 16a) similar to those observed during the Yaquina Bay experiment (figure 5a - b). This is in agreement with previous field observations (BERNER, 1963; JØRGENSEN and FENCHEL, 1974), indicating that in anoxic marine sediment, sulfide will regulate the potential difference with seawater. Further evidence was given by Allen and Hickling (1957) who attributed a measured half cell voltage of -0.5 V (vs. a saturated calomel reference) at open circuit to the equilibrium potential of a sulfur - sulfide system under alkaline conditions. The current density produced by the laboratory experiments (figure 16b) was comparable to levels produced by the device deployed under natural conditions (figure 5d). This confirms that sulfide can play an important role in the fuel cell mechanism, even if bacteria are also contributing to the energy production (BOND et al., 2002; BOND and LOVLEY, 2003).

Other studies have reported the direct oxidation of sulfide from chloride brines at graphite electrodes under extreme anodic conditions (+0.45 V vs. Ag/AgCl) applied for a short time (3.6 hrs) (ATEYA and ALKHARAFI, 2002b; ATEYA et al., 2003). The laboratory fuel cell simulations produced current density records similar to the brines work, despite the differences in voltage and in experiment duration. The current increased when sulfide was added to the system (figure 16b). This indicates that HS^- oxidation is controlled by charge transfer at the electrode/electrolyte interface and by

diffusion from within the electrolyte across the electrode double layer (ATEYA and ALKHARAFI, 2002b). The early exponential decay of current with time can be attributed to passivation of the electrode surface (ATEYA et al., 2003), rather than a reduction in the sulfide flux due to consumption of HS⁻. The diurnal oscillations exhibited by the current density (figure 16b) were probably a consequence of changes in light or/and temperature. Such variations were also observed during the Yaquina Bay experiment. Ateya et al. (2003) demonstrated that temperature influences the rate of sulfide oxidation: lower temperature (e.g. at night) resulted in a decrease in current. Thus physical parameters influence the kinetics of electrochemical reactions, which is reflected in the number of electrons that is exchanged.

IV.3. Electrochemical reactivity of sulfide minerals

The redox chemistry of sulfide species in marine environments is complicated by the high reactivity of sulfur and its multiple oxidation states. Ateya et al. (2003) discuss that several products may be formed by electrochemical oxidation of sulfide:



Values of E^0 represent standard reduction potentials.

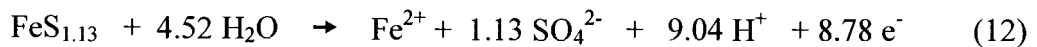
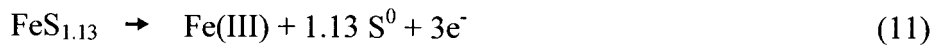
This study demonstrated that at least some of these sulfur transformations also occurred at the anode of the seafloor fuel cells deployed in Yaquina Bay, OR and in the Tuckerton salt marsh, NJ (figures 6a, 7 and 9e).

Initially it seems likely that the supply of HS⁻ to the anode is limited by its porewater concentration (modulated by the activity of sulfate-reducing bacteria and reactions with iron) and its diffusion in porewater. Then other sources of reductant may interact to continuously sustain the current production (Figure 5d). Figure 8e - f and figure 10a - b show that reduced sulfur minerals also react under the effects of the fuel cell. The dissolution of these compounds by oxidation may provide electrons to the electrode sustaining the production of electricity. A probable hypothesis, related to the

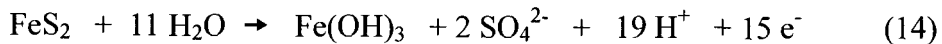
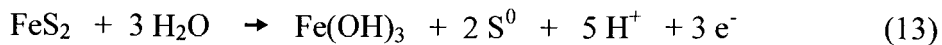
semi-conductor properties of AVS and pyrite, suggests that electrons could be shuttled along the mineral grains to the electrodes.

Hamilton and Woods (1981) reported that the electrochemical oxidation of iron sulfide and pyrite under alkaline conditions results in the formation of elemental sulfur and sulfate ions according to the following reactions:

Iron sulfide:



Pyrite:



FeS oxidation corresponding to reactions (10) or (12) could explain why porewater profiles exhibited an enrichment in Fe(II) at the anode surface (figure 6c and 9c).

IV.4. Elemental sulfur as an oxidation product

The surface analysis of the anodes of the laboratory and field fuel cells revealed a film of sulfur deposited at the electrode surface (figures 12d, 13d, 14a, 17d, and 18a). The only solid-phase compound produced by sulfide oxidation is elemental sulfur (reactions (5) and (6)). Ateya et al. (2003) used X-ray Photoelectron Spectroscopy to identify S^0 as the product of the electrochemical oxidation of sulfide on graphite electrodes. This is in agreement with a mechanism proposed by Allen and Hickling (1957) who suggested that the rate-determining step of sulfide oxidation on an inert electrode is the adsorption of uncharged sulfur at the electrode surface. Elemental sulfur is also the dominant product of the electrochemical oxidation of sulfide minerals (reactions (10) and (13)) (HAMILTON and WOODS, 1981). Mc Guire et al. (2001) have verified the formation of S^0 on pyrite mineral grains during oxidation within the natural environment.

By converting the electrical current record (figure 5d) to moles of electrons consumed, and comparing this value to estimates of the total decrease of reduced sulfur species (HS^- , FeS, FeS₂) (figures 6a, 8e and 8f), further insight may be gained into the

electron transfer mechanism to the anode in Yaquina Bay. The integration of the current produced during the 7-month experiment in Yaquina Bay corresponds to a transfer of 2.23 moles of electrons. The planar geometry of the electrodes suggests that similar reactions occurred on both faces of the disc. For the Oregon experiment we examined only the composition of sediments above the anodes; thus we assume these geochemical changes were associated with reactions passing 1.115 moles of electrons. Significant concentration gradients in solid-phase iron and sulfur species started 3 cm above the active anode (figures 6 and 8). Thus this seems to define a critical sediment reaction layer for the Oregon experiment with a volume of $4.11 \times 10^{-3} \text{ m}^3$. Then it is possible to estimate the amount of reduced sulfur oxidized within this volume by integrating the linear concentration gradients of reduced sulfur species (Appendix A). By this approach, the solid-phase profiles from Yaquina Bay predict a loss of 74 mmoles of pyrite (figure 8f) and 72 millimoles of AVS (figure 8e) (Appendix A).

The consumption of dissolved species is more difficult to estimate because porewater distributions probably varied over the seven month experiment. If Fick's first law of diffusion is applied using the sulfide gradient extending 10 cm from the anode at the end of the experiment, and a diffusion coefficient for sulfide through sediment of $1.3 \times 10^{-5} \text{ cm}^2/\text{s}$ (BOUDREAU, 1997), only 5 to 10 millimoles of dissolved sulfide would have been consumed (Appendix A), corresponding to a contribution of 10 to 20 millimoles of electrons according to the reaction (5). These calculations indicate that sulfide minerals were probably the dominant source of electrons to the anode. Based on reactions (10) and (13), the losses of AVS (i.e. FeS) and pyrite should have produced in total 366 millimoles of electrons and 229 millimoles of elemental sulfur. Turcotte et al. (1993) and Zhu et al. (1994) argued that elemental sulfur resulting from pyrite oxidation is an electrochemical form of sulfur unlike bulk S^0 in its orthorhombic state. This means that S^0 can be further oxidized or reduced, depending on the potential conditions. The applied potential, in addition to the pH of the medium, determines the reactivity of elemental sulfur.



Elemental sulfur oxidation may also be microbially mediated: Holmes et al. (2004) demonstrated the ability of *Desulfobulbus propionicus*, a representative of the family

Desulfobulbaceae, to oxidize S^0 to SO_4^{2-} with an electrode serving as an electron acceptor. In order to balance the electrons transferred to the anode, 54 % of the elemental sulfur produced by the oxidation of the sulfide minerals must have been further oxidized to sulfate (Appendix A). The remaining 46% of S^0 (105 millimoles) could have become available for microbial activity or could have accumulated. This amount of elemental sulfur would correspond to an average enrichment of $24 \mu\text{mol } S^0/\text{g}$ dry sediment in the 3 cm thick sediment layer above the anode. Certainly some enrichment was detected by electron microprobe analysis, with accumulation of sulfur at the electrode surface (figures 12d and 13d). Moreover X-ray maps indicate a dilution effect as a function of the distance from the anode, with a sulfur concentration in the biofilm about four times lower than at the electrode surface.

IV.5. Other chemical consequences of sulfide mineral oxidation

The oxidation of sulfide minerals is a mechanism that can enrich the environment surrounding the anode in Fe^{2+} ions (reaction (10)) and solid Fe oxyhydroxide $Fe(OH)_3$ (reaction (13)). At both sites (Yaquina Bay and Tuckerton), porewater analysis showed significant increases in dissolved iron concentrations at the active anode surface (1 mM in Yaquina Bay (figure 6c) and $14 \mu\text{M}$ in Tuckerton (figure 9g)), but not at the control anode. Surface analysis also indicated deposition of Fe at the electrode surface (figures 12b, 13e and 14b). The iron enrichment corresponded to areas where oxygen and sulfur were higher (figure 12c - d). The distribution of these three elements is further evidence of the oxidation of pyrite by the fuel cell (reaction (13)) leading to the formation of S^0 and $Fe(OH)_3$ that accumulate at the anode surface. This is also consistent with depletion of phosphate in porewater approaching the active anode (figures 6g and 9d) and with higher concentrations of solid phase phosphorus at the graphite surface (figure 13b). Rozan et al. (2002) reported that PO_4^{3-} adsorbs onto iron oxides.

IV.6. Consequences of sulfur deposition

It is possible to estimate the maximum thickness of a S^0 -film that would deposit uniformly at an electrode surface based on the number of electrons transferred during

the experiment. In this approximation the molecular arrangement of sulfur is assumed to resemble singular atoms stacked in simple monolayers. Previous calculations indicated that a maximum of 105 mmol of elemental sulfur may have been deposited on half of the surface area of the electrode during the Yaquina Bay experiment. Assuming an atomic radius of S equal to 1.09×10^{-10} m, then the maximum thickness of a film of only S^0 would be 7.3 μm (Appendix B). Microprobe analyses (figure 12d and 13d) showed a sulfur enrichment corresponding to a layer of about 20 μm and a sulfur concentration of only 2 wt % at the most in this layer.

The surface analyses of the Yaquina Bay anode also revealed the presence of iron (figures 12b and 13e), phosphorus (figure 13b), silicon (figure 13c) and oxygen (figure 12c). Because sulfide sources may have varied over time and the Yaquina Bay anode had periods of inactivity, S^0 deposition may have alternated with periods of biofilm growth and deposition of other compounds, like Fe oxides and adsorbed phosphate, resulting in a thicker layer compared to the theoretical estimation. Moreover, as discussed above, elemental sulfur may have been only an intermediate in the oxidation of sulfide. According to Allen and Hickling (1957), the properties of the sulfur layer formed at the electrode surface depend on the current density and so also on the applied potential difference. What is not yet known is to what degree the coatings seen on the active fuel cell anodes affected the rate of the electron transfer. In other words, it is not known if passivation severely limits electron flow after long periods of sediment fuel cell activity.

The current produced by the laboratory fuel cell also resulted from sulfide oxidation. The current integration over time and the conversion to moles of electrons was used to estimate that 64.7 μmol of S^0 was produced according to reaction (5). By similar reasoning to that applied for the Yaquina Bay experiment, a 0.64 μm -thick film of sulfur should have deposited on the laboratory electrode (Appendix B). This is thinner than the microprobe beam size used for the surface analyses. However figure 17 indicates a thin layer of S on the electrode surface that was not uniformly distributed. This is in agreement with the sulfide oxidation mechanism described by Allen and Hickling (1957), with irregular elemental sulfur adsorption on the electrode surface. McGuire et al. (2001) have also reported that elemental sulfur as product of the

oxidation of reduced sulfur does not form a continuous film, but deposits as discrete patches, dispersed randomly across the sample surface.

IV.7. Biogeochemical cycle of sulfur

The purpose of this study was to determine whether the main mechanism of electron transfer at the seafloor fuel cell anode was microbial or electrochemical. By reconciling the geochemical effects of the fuel cell with the microbial analyses it seems likely that a unique biogeochemical cycle was created or amplified, at least in the case of the Yaquina Bay experiment.

The cycle (figure 19) was possible because organic matter is degraded nearly continuously by sulfate-reducing bacteria in the anoxic sediment of Yaquina Bay. This anaerobic metabolism enriches the environment in dissolved sulfide. Part of the sulfide reacts with Fe oxides to produce S^0 , FeS, FeS₂ (reactions (3) and (4)) and these minerals accumulate with sediment depth. In the presence of the active fuel cell, sulfide became electroactive at the anode surface. Elemental sulfur is indicated to be the main end product of this electrochemical sulfide oxidation, because of the sulfur accumulation at the active anode surface (figures 12d, 13d, 14a, 17d, and 18a) and also because of the dominant abundance of *Desulfobulbus* and *Desulfocapsa* spp. (table 1) which are known to disproportionate elemental sulfur when the level of sulfide is low. The conversion of current to moles of electrons and the integration of profile gradients indicated that the consumption of dissolved sulfide alone was not sufficient to sustain the current production. However analyses of solid-phase distributions showed a decrease of AVS (figure 8e) and pyrite (figure 8f) toward the anode. The reduced sulfur minerals were probably oxidized according to the reactions (10) and (13), producing elemental sulfur. To balance the current production, part of the S^0 must have been further oxidized to sulfate (reaction (15)), supplying more electrons to the electrical circuit. This reaction may be abiotic (TURCOTTE et al., 1993; ZHU et al., 1994) and/or microbially mediated (HOLMES et al., 2004) and returns SO_4^{2-} to the sediments surrounding the anode. As a consequence of the dissolution of sulfide minerals, Fe^{2+} was released and accumulated near the anode surface (figure 6c). Some iron may have precipitated as Fe oxides (reaction (13)), coating the graphite surface with a thin layer

Figure 19: Biogeochemical cycle amplified by the fuel cell mechanism.

— Electrochemical reaction; ▨ sulfate-reducing bacteria;

▤ S^0 -disproportionation; — geochemical reactions

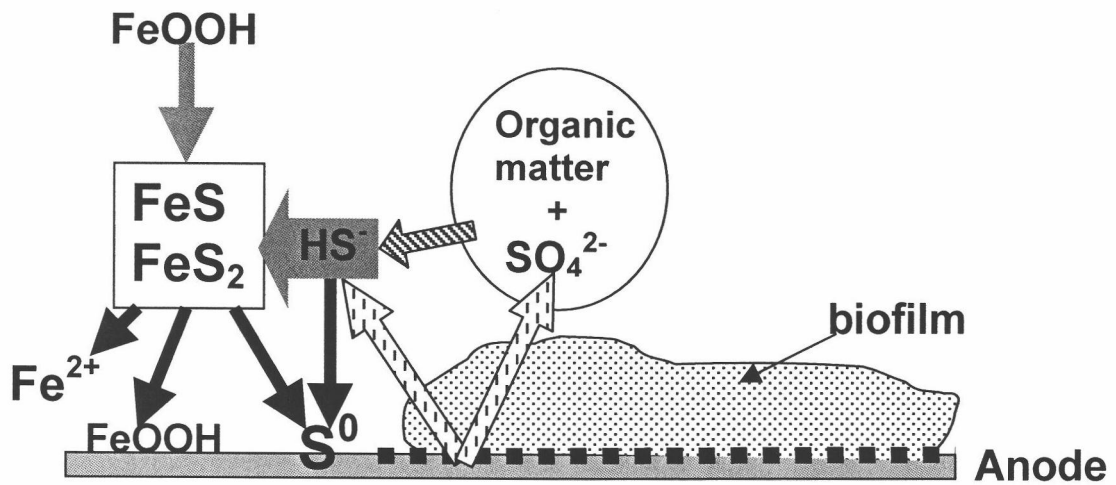


(figure 12b, 13e, 14b). The cycle was completed when part of the elemental sulfur was disproportionated by the biofilm bacteria to produce sulfide and sulfate.

In comparison to the Yaquina Bay experiment, many of the same species of microorganisms were present on the Tuckerton anode and the geochemical profiles displayed similar patterns. This suggests that an analogous cycle was active in the salt marsh. The dominant abundance of bacteria in the Geobacteracea family also indicates that other electron transfer mechanisms can compete with this biogeochemical cycle. Recent studies (BOND et al., 2002; BOND and LOVLEY, 2003) demonstrated that these bacteria are able to grow using electrodes as terminal electron acceptors. Moreover laboratory experiments isolating microbial and electrochemical processes showed the capability of these pathways of electron production to generate electricity, individually. Microbial and electrochemical mechanisms are presumed to have coexisted in the Tuckerton experiment. However it is not yet possible to determine which one dominated the energy production, how vital is the interaction of these mechanisms, or how each mechanism may be controlled.

V. CONCLUSION

Fuel cells are devices that convert chemical energy directly to electrical energy. In the case of a seafloor fuel cell, the anode embedded in anoxic sediment acts as an electron acceptor. For the purpose of this study, electrodes were made of porous graphite. Two field experiments were conducted in coastal environments (the Yaquina Bay estuary, Oregon, and a salt marsh near Tuckerton, New Jersey), during approximately 7 months.

Biogeochemical and electrochemical processes occurring at the anode of the seafloor fuel cell were studied by analyzing changes in sediment composition and deposits on the anode surface. This approach helped to identify the most probable reactions influencing the buried electrode and to relate these reactions to the fuel cell mechanism.

The fuel cell prototypes measured a potential difference of 0.7 - 0.8 V at open circuit. This voltage gradient is regulated by the microbial activity that reduces sulfate to sulfide in the absence of oxygen. The selectivity of the fuel cell for groups of bacteria able to grow by transferring electrons directly to the electrode (BOND et al., 2002; BOND and LOVLEY, 2003) indicated one possible mechanism to generate electrical energy. However decreasing concentration gradients of dissolved HS^- and reduced sulfur minerals (FeS and FeS_2) suggested that reductants may also give electrons to the fuel cell by electrochemical oxidation. This hypothesis was confirmed by laboratory experiments simulating a fuel cell with HS^- as sole electron donor under sterile conditions. The current density produced by these small-scale electrochemical cells was comparable to the field data.

These electrochemical reactions induced by the seafloor fuel cell enriched the environment in elemental sulfur, ferrous iron, and iron (III) oxides, favoring the energy metabolism of the microorganisms that were identified from DNA extracted from the fuel cell anode (*Desulfobulbus/Desulfocapsa* and *Geobacteraceae*). The precipitation of S^0 and $\text{Fe}(\text{OH})_3$ formed a thin film that deposited on the anode and became associated with a biofilm. Sulfur deposition was also observed at the surface of the laboratory

electrodes. It is not yet known to what extent chemical and biological coatings may passivate the electrode reducing the rate of electron transfer.

The integration of the reductants consumed approaching the anode of the Yaquina Bay experiment showed that solid-phase FeS and FeS₂ were the dominant chemical electron donors to the fuel cell over the long term. The combination of the geochemical changes with the microbial selectivity suggests that a biogeochemical cycle contributes to the electricity production through the fuel cell anode. This cycle includes sulfate-reducing bacteria producing sulfide via organic matter decomposition, geochemical reactions of Fe oxides with dissolved HS⁻ to form sulfide minerals (FeS and FeS₂), and the electrochemical oxidation of sulfide, iron sulfide and pyrite depositing a film of elemental sulfur at the electrode surface and enriching the environment surrounding the anode in dissolved iron. The accumulation of S⁰ selects for groups of bacteria able to use elemental sulfur as electron donor or electron acceptor, producing sulfide and sulfate.

In conclusion, microbial and electrochemical processes participate in the transfer of electrons to the seafloor fuel cell anode. These two mechanisms coexist when fuel cells are run in a natural environment; however in the final analysis each are limited by the availability of reduced chemical species that can donate electrons to the electrode.

VI. BIBLIOGRAPHY

1. Allen P. L. and Hickling A. (1957) Electrochemistry of sulfur. Part 1 Overpotential in the discharge of the sulfide ion. *Transactions of the Faraday Society* **53**, 1626-1635.
2. Allen R. E. and Parkes R. J. (1995) Digestion procedures for determining reduced sulfur species in bacterial cultures and in ancient and recent sediments. In *Geochemical Transformations of Sedimentary Sulfur* (ed. M. A. Vairavamurthy and M. A. A. Schoonen), pp. 243-257. American Chemical Society.
3. Ateya B. G. and Alkharafi F. M. (2002a) Anodic oxidation of sulfide ions from chlorides brines. *Electrochemistry Communications* **4**, 231-238.
4. Ateya B. G. and Alkharafi F. M. (2002b) Electrochemical removal of hydrogen sulfide from geothermal brines. *Electrochemical Society Proceedings* **15**, 87-98.
5. Ateya B. G., Alkharafi F. M., and Al-Azab S. S. (2003) Electrodeposition of sulfur from sulfide contaminated brines. *Electrochemical and Solid-State Letters* **6**(9), C137-C140.
6. Baas Becking L. G. M., Kaplan I. R., and Moore D. (1960) Limits of the natural environment in terms of pH and oxidation-reduction potentials. *Journal of Geology* **68**(3), 243-284.
7. Bacon F. T. and Fry T. M. (1970) Review Lecture: the development and practical application of fuel cells. *Proceedings of the Royal Society of London. Series A, Mathematical and Physical Sciences* **334**(1599), 427-452.
8. Bard A. J. and Faulkner L. R. (2001) *Electrochemical Methods. Fundamentals and Applications*. 2nd Ed., John Wiley and Sons.
9. Beliaev A. S. and Saffarini D. A. (1998) *Shewanella putrefaciens mtrB* encodes an outer membrane protein required for Fe(III) and Mn(IV) reduction. *Journal of Bacteriology* **180**(23), 6292-6297.
10. Beliaev A. S., Saffarini D. A., McLaughlin J. L., and Hunnicutt D. (2001) MtrC, an outer membrane decahaem c cytochrome required for metal reduction in *Shewanella putrefaciens* MR-1. *Molecular Microbiology* **39**(3), 722-730.
11. Berner R. A. (1963) Electrode studies of hydrogen sulfide in marine sediments. *Geochimica et Cosmochimica Acta* **27**, 563-575.
12. Berner R. A. (1964) Stability fields of iron minerals in anaerobic marine sediments. *Journal of Geology* **72**, 826-834.

13. Berner R. A. (1970) Sedimentary pyrite formation. *American Journal of Science* **268**, 1-23.
14. Berner R. A. (1978) Sulfate reduction and the rate of deposition of marine sediments. *Earth and Planetary Science Letters* **37**, 492-498.
15. Berner R. A. (1984) Sedimentary pyrite formation: an update. *Geochimica et Cosmochimica Acta* **48**, 605-615.
16. Berner R. A. (1985) Sulfate reduction, organic matter decomposition and pyrite formation. *Philosophical Transactions of the Royal Society of London. Series A, Mathematical and Physical Sciences* **315**(1531), 25-37.
17. Bond D. R., Holmes D. E., Tender L. M., and Lovley D. R. (2002) Electrode-reducing microorganisms that harvest energy from marine sediments. *Science* **295**, 483-485.
18. Bond D. R. and Lovley D. R. (2003) Electricity production by *Geobacter sulfurreducens* attached to electrodes. *Applied and Environmental Microbiology* **69**(3), 1548-1555.
19. Boudreau B. P. (1997) *Diagenetic Models and Their Implementation. Modeling Transport and Reactions in Aquatic Sediments*. Springer.
20. Brendel P. J. and Luther III G. W. (1995) Development of a gold amalgam voltammetric microelectrode for the determination of dissolved Fe, Mn, O₂ and S(-II) in porewaters of marine and freshwater sediments. *Environmental Science and Technology* **29**(3), 751-760.
21. Canfield D. E. (1989a) Reactive iron in marine sediments. *Geochimica et Cosmochimica* **53**, 619-632.
22. Canfield D. E. (1989b) Sulfate reduction and oxic respiration in marine sediments: implications for organic carbon preservation in euxinic environments. *Deep-Sea Research* **36**(1), 121-138.
23. Canfield D. E., Raiswell R., Westrich J. T., Reaves C. M., and Berner R. A. (1986) The use of chromium reduction in the analysis of reduced inorganic sulfur in sediments and shales. *Chemical Geology* **54**, 149-155.
24. Castaneda F., Pezeron E., and Plichon V. (1987) Electrochemical oxidation of sulfide in presence of surfactants. *Bulletin de la Société Chimique de France* **1**, 34-36.
25. Cline J. D. (1969) Spectrophotometric determination of hydrogen sulfide in natural waters. *Limnology and Oceanography* **14**, 454-458.

26. Felderman T. G., Church T. M., and Luther III G. W. (1991) Sulfur enrichment of humic substances in Delaware salt marsh sediment core. *Geochimica et Cosmochimica* **55**, 979-988.
27. Finster K., Liesack W., and Thamdrup B. (1998) Elemental sulfur and thiosulfate disproportionation by *Desulfocapsa sulfoexigens* sp. nov., a new anaerobic bacterium isolated from marine surface sediment. *Applied and Environmental Microbiology* **64**(1), 119-125.
28. Fossing H. and Jørgensen B. B. (1989) Measurement of bacterial sulfate reduction in sediments: evaluation of a single-step chromium reduction method. *Biogeochemistry* **8-6**, 205-222.
29. Gaspard S., Vazquez F., and Holliger C. (1998) Localization and solubilization of the iron (III) reductase of *Geobacter sulfurreducens*. *Applied and Environmental Microbiology* **64**, 3188-3194.
30. Goldhaber M. B. and Kaplan I. R. (1975) Controls and consequences of sulfate reduction rates in recent marine sediments. *Soil Science* **119**(1), 42-55.
31. Greaves C. (1970) The direct conversion of chemical energy to electricity. *Physics Education* **5**(1), 18-24.
32. Hamilton I. C. and Woods R. (1981) An investigation of surface oxidation of pyrite and pyrrhotite by linear potential sweep voltammetry. *Journal of Electroanalytical Chemistry* **118**, 327-343.
33. Hernandez M. E. and Newman D. K. (2001) Extracellular electron transfer. *Cellular and Molecular Life Science* **58**, 1562-1571.
34. Holmes D. E., Bond D. R., and Lovley D. R. (2004) Electron Transfer by *Desulfobulbus propionicus* to Fe(III) and graphite electrodes. *Applied and Environmental Microbiology* **70**(2), 1234-1237.
35. Holmes D. E., Bond D. R., O'Neil R. A., Reimers C. E., Tender L. M., and Lovley D. R. (in press) Microbial communities associated with electrodes harvesting electricity from a variety of aquatic sediments. *Microbial Ecology*.
36. Janssen P. H., Schuhmann A., Bak F., and Liesack W. (1996) Disproportionation of inorganic sulfur compounds by the sulfate-reducing bacterium *Desulfocapsa thiozymogenes* gen. nov., sp. nov. *Archives of Microbiology* **166**, 184-192.
37. Jones D. A. (1996) *Principles and Prevention of Corrosion*. 2nd Ed., Princeton-Hall Inc.
38. Jørgensen B. B. (1977) The sulfur cycle of a coastal marine sediment (Limfjorden, Denmark). *Limnology and Oceanography* **22**(5), 814-832.

39. Jørgensen B. B. (1982) Ecology of the bacteria of the sulfur cycle with special reference to anoxic-oxic interface environments. *Philosophical Transactions of the Royal Society of London, series B.* **298**(1093), 543-561.
40. Jørgensen B. B. and Fenchel T. (1974) The sulfur cycle of a marine sediment model system. *Marine Biology* **24**, 189-201.
41. Keil R. G., Tsamakis E., Fuh C. B., Giddings J. C., and Hedges J. I. (1994) Mineralogical and textural controls on the organic composition of coastal marine sediments: hydrodynamic separation using SPLITT-fractionation. *Geochimica et Cosmochimica Acta* **58**(2), 879-893.
42. Kostka J. E. and Luther III G. W. (1994) Partitioning and speciation of solid iron in saltmarsh sediments. *Geochimica et Cosmochimica* **48**(7), 1701-1710.
43. Lin S., Huang K.-M., and Chen S.-K. (2002) Sulfate reduction and iron sulfide mineral formation in the southern East China continental slope sediment. *Deep-Sea Research* **49**, 1837-1852.
44. Lin S. and Morse J. W. (1991) Sulfate reduction and iron sulfide mineral formation in the Southern East China continental slope sediment. *American Journal of Science* **29**, 55-89.
45. Lovley D. R., Coates J. D., Blunt-Harris E. L., Phillips E. J. P., and Woodward J. C. (1996) Humic substances as electron acceptors for microbial respiration. *Nature* **382**, 445-448.
46. Lovley D. R. and Phillips E. J. P. (1994) Novel processes for anaerobic sulfate production from elemental sulfur by sulfate reducing bacteria. *Applied and Environmental Microbiology* **60**(7), 2394-2399.
47. Luther III G. W., Brendel P. J., Brent L. L., Sundby B., Lefrancois L., Silverberg N., and Nuzzio D. B. (1998) Simultaneous measurement of O₂, Mn, Fe, and S(-II) in marine pore waters with a solid-state voltammetric microelectrode. *Limnology and Oceanography* **43**(2), 325-333.
48. Luther III G. W., Glazer B. T., Hohmann L., Popp J. L., Taillefert M., Rozan T. F., Brendel P. J., Theberge S. M., and Nuzzio D. B. (2001) Sulfur speciation monitored *in situ* with solid state gold amalgam voltammetric microelectrodes: polysulfides as a special case in sediments, microbial mats and hydrothermal vents water. *Journal of Environmental Monitoring* **3**, 61-66.
49. Luther III G. W., Reimers C. E., Nuzzio D., B., and Lovallo D. (1999) In situ deployment of voltammetric, potentiometric, and amperometric microelectrodes from a ROV to determine dissolved O₂, Mn, Fe, S(-2), and pH in porewaters. *Environmental Science and Technology* **33**, 4352-4356.

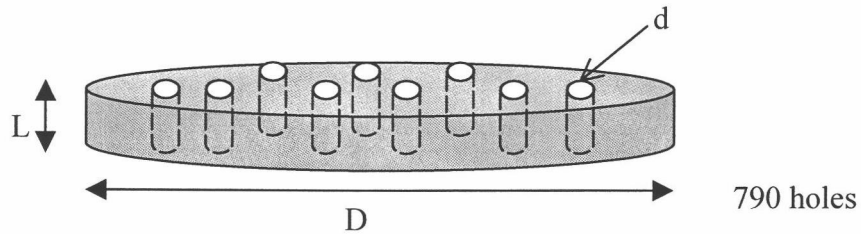
50. Magnuson S. T., Hodges-Myerson A. L., and Lovley D. R. (2000) Characterization of a membrane-bound NADH-dependent Fe(III) reductase from the dissimilatory Fe(III)-reducing bacterium *Geobacter sulfurreducens*. *FEMS Microbiology Letters* **185**, 205-211.
51. McDougall A. (1976) *Fuel cells*. Wiley & Sons.
52. McGuire M. M., Jallad K. N., Ben-Amotz D., and Hamers R. J. (2001) Chemical mapping of elemental sulfur on pyrite and arsenopyrite surfaces using near-infrared Raman imaging microscopy. *Applied Surface Science* **178**, 105-115.
53. Measures C. I., Yuan J., and Resing J. A. (1995) Determination of iron in seawater by flow injection-analysis using in-line preconcentration and spectrophotometric detection. *Marine Chemistry* **50**, 3-12.
54. Müller P. J. and Suess E. (1979) Productivity, sedimentation rate, and sedimentary organic matter in the oceans - I. Organic carbon preservation. *Deep-Sea Research* **26A**, 1347-1362.
55. Myers C. R. and Myers J. M. (1992) Localization of cytochromes to the outer membrane of anaerobically grown *Shewanella putrefaciens* MR-1. *Journal of Bacteriology* **174**(11), 3429-3438.
56. Nevin K. P. and Lovley D. R. (2000) Lack of production of electron-shuttling compounds or solubilization of Fe(III) during reduction of insoluble Fe(III) oxide by *Geobacter metallireducens*. *Applied and Environmental Microbiology* **66**, 2248-2251.
57. Nevin K. P. and Lovley D. R. (2002) Mechanisms for Fe(III) oxide reduction in sedimentary environments. *Geomicrobiology Journal* **19**, 141-159.
58. Pfenning N. and Biebl B. (1976) *Desulfuromonas acetoxidans* gen. nov. and sp. nov., a new anaerobic, sulfur-reducing, acetate-oxidizing bacterium. *Archives of Microbiology* **110**, 3-12.
59. Pokrovski G. S., Schott J., Farges F., and Hazemann J.-L. (2003) Iron (III)-silica interactions in aqueous solution: insights from X-ray absorption fine structure spectroscopy. *Geochimica et Cosmochimica Acta* **67**(19), 3559-3573.
60. Powell H. S. (1980) Decomposition of organic matter in estuarine sediments by sulfate reduction : a field study from Yaquina Bay and sediment incubation experiments. Masters Thesis, Oregon State University.
61. Pysik A. J. and Sommer S. E. (1981) Sedimentary iron monosulfides: kinetics and mechanism of formation. *Geochimica et Cosmochimica Acta* **45**, 687-698.

62. Ransom B., Kim D., Kastner M., and Wainwright S. (1998) Organic matter preservation on continental slopes: importance of mineralogy and surface area. *Geochimica et Cosmochimica Acta* **62**(8), 1329-1345.
63. Reimers C. E., Tender L. M., Fertig S. J., and Wang S. (2001) Harvesting energy from the marine sediment-water interface. *Environmental Science and Technology* **35**, 192-195.
64. Resing J. A. and Mottl M. J. (1992) Determination of manganese in seawater using flow injection analysis with on-line preconcentration and spectrophotometric detection. *Analytical Chemistry* **64**, 2682-2687.
65. Roden E. E. and Lovley D. R. (1993) Dissimilatory Fe(III) reduction by the marine microorganism *Desulfuromonas acetoxidans*. *Applied and Environmental Microbiology* **59**(3), 734-742.
66. Rozan T. F., Taillefert M., Trouwborst R. E., Glazer B. T., and Ma S. (2002) Iron-sulfur-phosphorous cycling in the sediments of a shallow coastal Bay: implications for sediment nutrient release and benthic macroalgal blooms. *Limnology and Oceanography* **47**(5), 1346-1354.
67. Rozan T. F., Theberge S. M., and Luther III G. W. (2000) Quantifying elemental sulfur (S^0), bisulfide (HS^-) and polysulfides (S_x^{2-}) using a voltammetric method. *Analytica Chimica Acta* **415**, 175-184.
68. Scott D. T., McKnight D. M., Blunt-Harris E. L., Kolesar S. E., and Lovley D. R. (1998) Quinone moieties act as electron acceptors in the reduction of humic substances by humics-reducing microorganisms. *Environmental Science and Technology* **32**(19), 2984-2989.
69. Seeliger S., Cord-Ruwish R., and Schink B. (1998) A periplasmic and extracellular c-type cytochrome of *Geobacter sulfurreducens* acts as a ferric iron reductase and as an electron carrier to other acceptors or to partner bacteria. *Journal of Bacteriology* **180**(14), 3686-3691.
70. Shih Y.-S., Kuo S.-L., and Cheng C.-W. (1989) Experimental analysis of flow-by and flow-through extractive reactors for the electrochemical oxidation of sulfide ion to sulfur. *Journal of the Chinese Institute of Chemical Engineers* **20**(6), 365-373.
71. Stookey L. L. (1970) Ferrozine - A new spectrophotometric reagent for iron. *Analytical Chemistry* **42**(7), 779-781.
72. Straub K. L., Benz M., and Schink B. (2001) Iron metabolism in anoxic environments at near neutral pH. *FEMS Microbiology Ecology* **34**, 181-186.

73. Tender L. M., Reimers C. E., Stecher III H. W., Holmes D. E., Bond D. R., Lowy D. A., Pilobello K., Fertig S. J., and Lovley D. R. (2002) Harnessing microbially generated power on the seafloor. *Nature Biotechnology* **20**, 821-825.
74. Thamdrup B. and Canfield D. E. (1996) Pathways of carbon oxidation in continental margin sediments off central Chile. *Limnology and Oceanography* **41**(8), 1629-1650.
75. Thamdrup B., Finster K., Hansen J. W., and Bak F. (1993) Bacterial disproportionation of elemental sulfur coupled to chemical reduction of iron or manganese. *Applied and Environmental Microbiology* **59**(1), 101-108.
76. Thamdrup B., Fossing H., and Jørgensen B. B. (1994) Manganese, iron and sulfur cycling in a coastal marine sediment, Aarhus Bay, Denmark. *Geochimica et Cosmochimica Acta* **58**, 5115-5129.
77. Turcotte S. B., Benner R. E., Riley A. M., Li J., Wadsworth M. E., and Bodily D. M. (1993) Surface analysis of electrochemically oxidized metal sulfides using Raman spectroscopy. *Journal of Electroanalytical Chemistry* **347**, 195-205.
78. Verardo D. J., Froelich P. N., and Andrew M. (1990) Determination of organic carbon and nitrogen in marine sediments using the Carlo Erba NA-1500 analyzer. *Deep-Sea Research* **37**(1), 157-165.
79. Vijn A. K. (1970) Electrochemical principles involved in a fuel cell. *Journal of Chemical Education* **47**(10), 680-682.
80. Walsh J. J., Premuzic E. T., Gaffney J. S., Rowe G. T., Hartbottle G., Stoenner R. W., Balsam W. L., Betzer P. R., and Macko S. A. (1985) Organic storage of CO₂ on the continental slope off the mid-Atlantic bight, the southeastern Bering Sea, and the Peru coast. *Deep-Sea Research* **32**(7), 853-883.
81. Wang Q. and Morse J. W. (1996) Pyrite formation under conditions approximating those in anoxic sediments. I. pathway and morphology. *Marine Chemistry* **52**, 99-121.
82. Wijsman J. W. M., Middelburg J. J., Herman P. M. J., Böttcher M. E., and Heip C. H. R. (2001) Sulfur and iron speciation in surface sediments along the northwestern margin of the Black Sea. *Marine Chemistry* **74**, 261-278.
83. Zhabina N. N. and Volkov I. I. (1978) A method of determination of various sulfur compounds in sea sediments and rocks. In *Environmental Biogeochemistry: Methods, metals and assessment*, Vol. 3 (ed. W. E. Krumbein), pp. 735-745. Ann Arbor Science Publishers.
84. Zhu X., Li J., and Wadsworth M. E. (1994) Characterization of surface layers formed during pyrite oxidation. *Colloids and Surfaces A: Physicochemical and Engineering Aspects* **93**, 201-210.

APPENDICES

Appendix A: Integration of the concentration gradients and conversion to moles of electrons



➤ Field electrode

$D = 48.3 \text{ cm}$ (diameter of the electrode)

$L = 1.3 \text{ cm}$ (thickness of the electrode)

$d = 0.64 \text{ cm}$ (diameter of one hole)

electrode surface: $A_F = \pi DL + 2\pi*(D/2)^2 - 790*\pi*(d/2)^2 + 790*\pi dL$
 5672.5 cm^2

surface of one face of the electrode: $S = \pi*(D/2)^2$
 1832 cm^2

volume of holes: $v = 790* \pi*(d/2)^2*L$
 330 cm^3

➤ Volume of a sediment layer covering the electrode:

(sediment thickness) $l = 3 \text{ cm}$

$$V = l*S + v/2$$

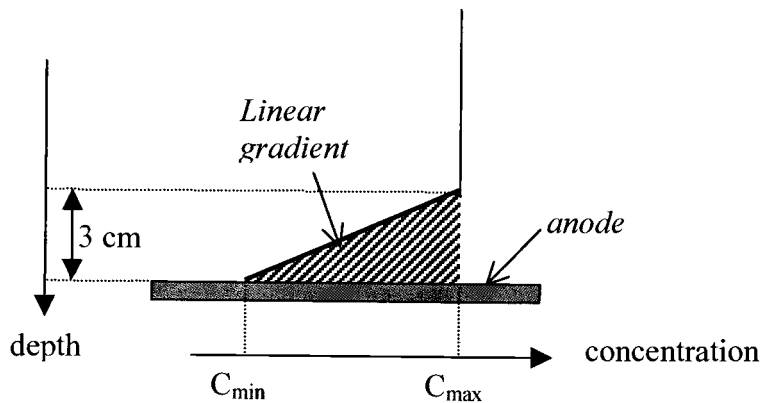
$$5661 \text{ cm}^3$$

porosity: $P = 70\%$

volume of solid phase $V_{SP}: V_{SP} = (1-P)*V = 1698 \text{ cm}^3$

solid phase density: $\rho = 2.5\text{g}/\text{cm}^3$

➤ Integration of the concentration gradients:



✓ For solid phase:

$$n = V_{SP} \cdot \rho \cdot (C_{max} - C_{min}) / 2$$

with n = number of moles of compound that was consumed

V_{SP} = volume of solid phase in the sediment layer

ρ = solid phase density

C_{max} = maximal concentration

C_{min} = minimal concentration

AVS: decrease from [51 ; 57] $\mu\text{mol S/g}$ dry sediment to [16.6 ; 23.5] $\mu\text{mol S/g}$ dry sediment

$$n_{\text{FeS}} = n(\text{S})_{\text{AVS}} = 58 - 86 \text{ mmol}$$

$$n_{\text{FeS}}(\text{average}) = 72 \text{ mmol}$$

Pyrite: decrease from [181 ; 219] $\mu\text{mol S/g}$ dry sediment to [114 ; 146] $\mu\text{mol S/g}$ dry sediment

$$n_{\text{FeS}_2} = n(\text{S})_{\text{pyrite}} / 2 = 37 - 111 \text{ mmol}$$

$$n_{\text{FeS}_2}(\text{average}) = 74 \text{ mmol}$$

✓ For dissolved compounds:

Using Fick's first law of diffusion

$$q = D_{\text{HS}^-} \cdot x \cdot (C_{max} - C_{min}) / l$$

and

$$n = q \cdot t \cdot x \cdot S$$

with q = Flux

D_{HS^-} = diffusion coefficient of sulfide through sediment

l = thickness of the sediment layer subject to sulfide diffusion

C_{max} = maximal concentration

C_{min} = minimal concentration

n = number of moles of compound that was consumed

t = time corresponding to the diffusion

S = surface of one face of the electrode

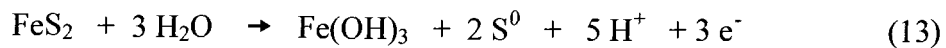
Sulfide: decrease from [113 ; 220] μM to 0 μM

$$D_{HS^-} = 1.3 \cdot 10^{-5} \text{ cm}^2/\text{s}$$

$n_{HS^-} = 5 - 10 \text{ mmol}$ *negligible compare to AVS and pyrite consumption, because it would produce only 10 - 20 mmol e^- (reaction (5)).*

➤ Electrons and elemental sulfur production

✓ Oxidation of sulfide minerals:



AVS: production of **144 mmol e^-** and **81 mmol S^0**

Pyrite: production of **222 mmol e^-** and **148 mmol S^0**

In total: production of **366 mmol e^-** and **229 mmol S^0**

✓ Elemental sulfur oxidation:



Percent of S^0 oxidized:

$$(n_{e^-}(\text{total}) - n_{e^-}(\text{minerals})) \times 100 / (n_{e^-}(\text{S}^0) \times n_{\text{S}^0}) = (1115 - 366) \times 100 / (6 \times 229) = 54 \%$$

Oxidation of 54% S^0 produced from minerals oxidation.

concentration of S⁰:

$$n(S^0) = 46 \% \times 229 = \mathbf{105 \text{ mmol}}$$

$$C(S^0) = n(S^0) / (V_{SP} * \rho) = \mathbf{25 \text{ } \mu\text{mol S/g dry sediment}}$$

➤ Conversion of current to moles of electrons: 1 Amp = 96500 mol e⁻/sec

Appendix B: Elemental sulfur deposition

Sulfur

atomic radius: $r = 1.09 \cdot 10^{-10}$ m

atom surface: $s = 4\pi r^2 = 1.49 \cdot 10^{-19}$ m²/at S

➤ Laboratory electrode

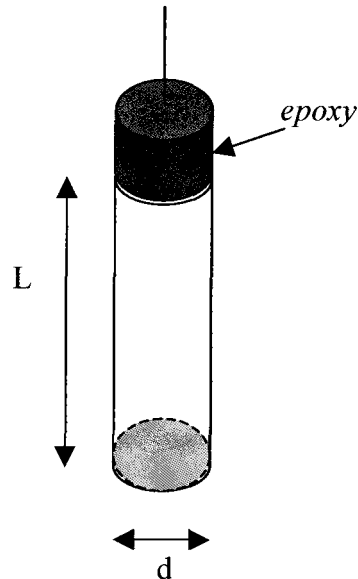
$L = 48.5$ mm (length of the electrode)

$d = 12.5$ mm (diameter of the electrode)

- electrode surface:

$$A_L = \pi dL + \pi \cdot (d/2)^2$$

$$\mathbf{2026 \text{ mm}^2}$$



- maximum number of moles elemental sulfur deposited on the electrode:

$$n_{\text{tot}}(\text{S}) = \mathbf{64.7 \text{ } \mu\text{mol}}$$

- moles of S per monolayer:

$$n_{\text{mono}}(\text{S}) = A_L/s = \mathbf{0.0225 \text{ } \mu\text{mol}}$$

- number of layers corresponding to the maximum amount of produced S⁰:

$$n_{\text{layer}} = n_{\text{tot}}(\text{S})/n_{\text{mono}}(\text{S}) = \mathbf{2875 \text{ layers}}$$

- thickness of the S⁰-film (assuming monolayers):

$$t = n_{\text{layer}} \cdot 2r = \mathbf{0.627 \text{ } \mu\text{m}}$$

➤ Field electrode

- electrode surface: $A_F = \mathbf{5672.5 \text{ cm}^2}$

- maximum number of moles elemental sulfur deposited on the electrode:

$$n_{\text{tot}}(\text{S}) = \mathbf{105 \text{ mmoles}}$$

This corresponds to only half of the current, so it covers half of the electrode surface.

- moles of S per monolayer, covering half of the electrode:

$$n_{\text{mono}}(\text{S}) = A_{\text{F}}/2s = \mathbf{3.15 \mu\text{mol}}$$

- number of layers corresponding to the maximum amount of produced S^0 :

$$n_{\text{layer}} = n_{\text{tot}}(\text{S})/ n_{\text{mono}}(\text{S}) = \mathbf{33333 \text{ layers}}$$

- thickness of the S^0 -film (assuming monolayers):

$$t = n_{\text{layer}} * 2r = \mathbf{7.3 \mu\text{m}}$$

Appendix C: Porewater data from the Yaquina Bay experiment

sample	distance from electrode (cm)	Depth below water-sediment interface (cm)	NH ₄ ⁺ (μM)	Standard deviation n=2 ³	Cl ⁻ (mM)	Standard deviation n=2 ³	Fe (μM)	Standard deviation n=2 ³
Surface of the active anode	0	-20	1952		501.4		1060.3	
	0	-20	1053		474.2		695.4	
Core above the active anode	0.5	-19.5	1841		487.2		539.2	
	1.5	-18.5	2369		489.8		245.3	
	2.5	-17.5	3055		470.7		43.5	
	3.5	-16.5	2117		476.0		10.9	
	4.5	-15.5	2204		475.7		6.1	
	6	-14	1641	22	467.5	1.4	6.3	3.3
	8	-12	1120	9	459.8	0.6	5.1	0.9
	10	-10	652	43	449.1	0.2	2.0	0.4
	12	-8	348	11	450.0	2.0	2.0	0.3
	14	-6	168	14	431.0	0.6	42.5	3.7
	16	-4	128		431.5		61.7	
	17.5	-2.5	115		433.7		48.5	
	18.5	-1.5	106		433.0		91.7	
19.5	-0.5	87		437.8		54.3		
21	+1	27		439.5		0.5		
Core above the control anode	5.25	-14.75	281		441.9		10.5	
	6.5	-13.5	270		438.7		4.6	
	7.5	-12.5	239		438.4		3.8	
	8.5	-11.5	270		439.2		2.5	
	9.5	-10.5	251		435.9		1.6	
	11	-9	252		440.6		1.0	
	13	-7	258	18	439.0	1.3	2.2	0.4
	15	-5	281	6	424.3	10.4	3.6	0.2
	17	-3	206	7	431.5	1.3	47.2	5.3
19	-1	84		430.2		28.8		
Core along the control cell	-0.25	-20.25	294		451.3		6.9	
	1.25	-18.75	308		454.3		7.4	
	3	-17	289	16	450.4	1.9	12.8	3.3
	5	-15	284		451.3		12.1	
	7	-13	263	14	435.0	4.8	14.2	1.6
	9	-11	248	7	438.5	5.1	16.7	7.8
	11	-9	269	22	428.8	3.1	6.4	2.4
	13	-7	260	53	445.4	6.8	5.2	2.0
	15	-5	243	7	429.6	8.5	2.6	0.0
	17	-3	143	14	424.7		11.8	0.1
	19	-1	68		431.5		28.6	
21	+1	23		436.3		0.4		

³ Duplicate sediment samples from the same interval

Sample	distance from electrode (cm)	Depth below water-sediment interface (cm)	PO ₄ ³⁻ (μM)	Standard deviation n=2 ³	SO ₄ ²⁻ (mM)	Standard deviation n=2 ³	S ²⁻ (μM)	Standard deviation n=2 ³
Surface of the active anode	0	-20	12		16.9		0.0	
	0	-20	19		18.3		0.0	
Core above the active anode	21	-19.5	2		21.5		0.0	
	19.5	-18.5	9		21.8		0.0	
	18.5	-17.5	17		21.4		0.0	
	17.5	-16.5	17		21.0		0.0	
	16	-15.5	11		20.8		0.0	
	14	-14	29	3	20.7	0.3	0.1	0.0
	12	-12	55	2	21.4	0.6	113.9	15.8
	10	-10	120	8	20.2	0.6	166.5	53.6
	8	-8	203	10	19.1	0.2	64.6	14.6
	6	-6	208	5	16.2	0.1	53.4	47.6
	4.5	-4	178		15.3		19.4	
	3.5	-2.5	220		14.5		5.3	
	2.5	-1.5	196		14.0		5.0	
1.5	-0.5	106		15.0		2.4		
0.5	+1	7		16.6		0.0		
Core above the control anode	19	-14.75	7		22.1		0.6	
	17	-13.5	23	4	20.8	0.0	0.6	0.6
	15	-12.5	48	2	20.0	1.1	68.7	
	13	-11.5	52	6	20.5	0.2	41.5	16.7
	11	-10.5	73		21.2		55.7	
	9.5	-9	93		21.0		57.2	
	8.5	-7	92		20.6		17.7	
	7.5	-5	75		20.0		9.8	
	6.5	-3	77		21.0		5.7	
5.25	-1	72		21.3		18.9		
Core along the control cell	21	-20.25	2		21.2		0.0	
	19	-18.75	5		22.4		0.2	
	17	-17	16	6	22.1	1.4	1.2	0.2
	15	-15	45	3	21.1	1.0	0.2	0.2
	13	-13	58	16	21.8	0.3	0.6	0.6
	11	-11	87	13	20.5	0.0	0.0	0.0
	9	-9	64	4	21.8	1.2	0.0	0.0
	7	-7	62	6	20.6	0.0	0.0	0.0
	5	-5	69		21.3		0.0	
	3	-3	74	6	21.3		0.0	0.0
	1.25	-1	91		20.5		0.9	
-0.25	+1	71		22.0		0.4		

sample	distance from electrode (cm)	Depth below water-sediment interface (cm)	Mn ²⁺ (μM)	Standard deviation n=2 ³	Si(OH) ₄ (μM)	Standard deviation n=2 ³
Surface of the active anode	0	-20	9.1		255.59	
	0	-20	7.2		191.22	
Core above the active anode	0.5	-19.5	9.3		63	
	1.5	-18.5	7.3		79	
	2.5	-17.5	5.1		91	
	3.5	-16.5	3.2		102	
	4.5	-15.5	1.8		89	
	6	-14	1.3	0.1	156	20
	8	-12	1.2	0.1	368	9
	10	-10	1.4	0.2	539	37
	12	-8	1.6	0.1	566	18
	14	-6	2.4	0.0	521	16
	16	-4	3.1		571	
	17.5	-2.5	8.0		463	
	18.5	-1.5	6.3		561	
	19.5	-0.5	4.9		545	
21	+1	2.0		235		
Core above the control anode	5.25	-14.75	1.1		121	
	6.5	-13.5	0.8		226	2
	7.5	-12.5	0.7		385	11
	8.5	-11.5	0.7		430	18
	9.5	-10.5	0.4		442	
	11	-9	0.4		500	
	13	-7	0.6	0.1	470	
	15	-5	4.0	0.6	428	
	17	-3	6.6	2.1	425	
19	-1	10.8		466		
Core along the control cell	-0.25	-20.25	1.4		52	
	1.25	-18.75	1.6		110	
	3	-17	1.8	0.4	278	32
	5	-15	2.0		487	36
	7	-13	1.7	0.0	431	93
	9	-11	1.3	0.5	493	33
	11	-9	1.3	0.1	458	3
	13	-7	1.7	0.3	467	4
	15	-5	2.2	0.6	460	
	17	-3	5.0	1.3	484	9
	19	-1	6.3		506	
21	+1	1.4		472		

Appendix D: Solid-phase data from the Yaquina Bay experiment

Sample	distance from electrode (cm)	Depth below water-sediment interface (cm)	AVS		pyrite	
			Concentration ($\mu\text{mol S/g dry sediment}$)	standard deviation $n=3^4$	Concentration ($\mu\text{mol S/g dry sediment}$)	standard deviation $n=3^4$
Core along the control cell	-0.25	-20.25	43.5	1.4	156	5
	1.25	-18.75	41.9	1.8	146	8
	3	-17	45.6	2.0	150	13
	5	-15	43.9	1.4	110	3
	7	-13	54.0	1.2	115	4
	9	-11	52.4	2.1	120	4
	11	-9	39.1	1.2	120	2
	13	-7	57.0	2.0	118	8
	17	-3	42.0	1.2	90	10
Surface of the active anode	0	20	16.6	0.3	114	6
	0	20	16.7	0.6	157	5
Core above the active anode	0.5	-19.5	23.5	1.3	142	4
	1.5	-18.5	31.1	1.9	183	14
	2.5	-17.5	53.9	3.1	200	19
	3.5	-16.5	49.5	2.6	171	13
	4.5	-15.5	54.8	2.0	174	8
	6	-14	59.0	2.3	134	5
	8	-12	71.3	3.5	138	8
	10	10	74.1	3.8	138	6
	14	-6	25.5	1.5	109	1
18.5	-1.5	1.6	0.1	67	6	

⁴ sediment samples were analyzed in triplicate

Sample	distance from electrode (cm)	Depth below water-sediment interface (cm)	Crystalline form		Amorphous form	
			Concentration ($\mu\text{mol S/g dry sediment}$)	Standard deviation $n=3^4$	Concentration ($\mu\text{mol S/g dry sediment}$)	standard deviation $n=3^4$
Core along the control cell	-0.25	-20.25	123	0	11.3	0.1
	1.25	-18.75	117	1	9.6	0.7
	3	-17	137	0	11.6	0.3
	5	-15	131	1	10.4	1.2
	7	-13	142	1	11.4	0.6
	9	-11	152	1	13.7	0.6
	11	-9	144	12	11.4	0.5
	13	-7	131	2	11.5	0.4
	17	-3	115	1	10.7	0.8
			165	1	26.2	1.1
Surface of the active anode	0	20	94	1	9.3	0.1
	0	20	119	1	10.2	0.3
Core above the active anode	0.5	-19.5	112	1	11.9	0.6
	1.5	-18.5	124	2	11.3	0.0
	2.5	-17.5	124	1	8.9	0.2
	3.5	-16.5	117	3	11.2	0.5
	4.5	-15.5	141	1	12.3	0.6
	6	-14	147	1	10.6	0.4
	8	-12	160	2	11.9	0.4
	10	10	170	1	13.0	0.5
	14	-6	216	1	24.1	0.5
	18.5	-1.5	271	3	70.7	1.1
19.5	-0.5	260	4	77.8	1.4	

Sample	distance from electrode (cm)	Depth below water-sediment interface (cm)	Organic carbon		Total Nitrogen	
			content (weight %)	standard deviation n=3 ⁴	content (weight %)	standard deviation n=3 ⁴
Core along the control cell	-0.25	-20.25	1.8	0.1	0.15	0.007
	1.25	-18.75	1.8	0.1	0.13	0.0007
	3	-17	1.7	0.2	0.16	0.02
	5	-15	1.7	0.0	0.14	0.008
	7	-13	1.9	0.3	0.15	0.002
	9	-11	1.9	0.0	0.17	0.01
	11	-9	2.0	0.0	0.16	0.003
	13	-7	1.7	0.0	0.15	0.01
	17	-3	1.8	0.0	0.16	0.01
			3.0	0.2	0.29	0.006
Surface of the active anode	0	20	1.7	0.2	0.15	0.01
	0	20	2.4	0.1	0.22	0.01
Core above the active anode	0.5	-19.5	2.0	0.1	0.19	0.002
	1.5	-18.5	2.2	0.3	0.18	0.001
	2.5	-17.5	2.2	0.2	0.18	0.002
	3.5	-16.5	2.2	0.3	0.19	0.001
	4.5	-15.5	2.2	0.2	0.20	0.02
	6	-14	2.1	0.1	0.21	0.02
	8	-12	2.2	0.1	0.20	0.004
	10	10	2.8	0.3	0.25	0.01
	14	-6	4.4	0.4	0.37	0.006
	18.5	-1.5	5.8	0.0	0.46	0.03
19.5	-0.5	5.2	0.0	0.48	0.04	

Appendix E: Porewater data from the Tuckerton experiment

	Slice (cm)	distance from the electrode (cm)	HS ⁻ (mM)	SO ₄ ²⁻ (mM)	Fe (μM)	Cl ⁻ (mM)	PO ₄ ³⁻ (μM)	Si(OH) ₄ (μM)	NH ₄ ⁺ (μM)
Active Cell									
Above Anode	0-0.5	0.25	0.06	13.9	14.71	403	54	595	1304
	0.5-1.0	0.75	0.14	14.7	1.91	433	56	573	1327
	1-1.5	1.25	0.37	14.3	0.49	444	57	564	1327
	1.5-2	1.75	0.54	13.3	0.23	430	59	558	1346
	2.0-3.0	2.5	0.67	12.9	0.20	427	59	574	1359
	3.0-4.0	3.5	0.98	12.9	0.53	430	61	555	1375
	4.0-5.0	4.5	1.00	12.7	0.51	430	72	552	1421
	5.0-6.0	5.5	1.59	11.7	0.05	433	80	530	1462
	6.0-7.0	6.5	1.72	10.7	0.15	424	86	524	1481
	7.0-8.0	7.5	1.94	11.2	0.07	426	94	524	1496
8.0-9.0	8.5	2.27	10.2	0.27	428				
Below Anode	0-0.5	-0.25	0.11	9.2	3.43	398	117	650	1696
	0.5-1.0	-0.75	0.11	10.2	1.63	452	120	576	1697
	1-1.5	-1.25	0.25	9.9	0.78	449	133	599	1709
	1.5-2	-1.75	0.57	8.8	0.35	440	136	577	1709
	2.0-3.0	-2.5	0.67	8.3	0.49	439	132	552	1715
	3.0-4.0	-3.5	0.94	7.7	0.47	436	126	501	1714
	4.0-5.0	-4.5	1.29	7.5	0.32	431	124	469	1729
	5.0-6.0	-5.5	0.95	7.8	0.32	438	124	447	1725
	6.0-7.0	-6.5	0.41	5.9		391			
Control Cell									
Above Anode	0.5-1.0	0.75	2.57	11.8	0.05	425	97	480	1492
	1-2	1.5	3.68	11.0	0.05	423	91	513	1476
	2-3	2.5	3.43	12.2	0.05	427	86	490	1474
	3-4	3.5	3.08	12.0	0.05	425	82	459	1397
	4-5	4.5	3.42		0.14		84	459	1407
	5-6	5.5	3.20	13.3	0.33	426	86	472	1385
	Below Anode	0-1.0	-0.5	3.19	6.6	0.55	420	141	533
1-2		-1.5	4.10	4.0	0.20	422	131	498	1631
2-3		-2.5	3.88	4.2	0.14	426	144	489	2249

Appendix F: Solid-phase data from the Tuckerton experiment

Sample	Distance from electrode (cm)	AVS		Pyrite	
		Concentration ($\mu\text{mol S / g dry sediment}$)	Standard deviation $n=3^5$	Concentration ($\mu\text{mol S / g dry sediment}$)	Standard deviation $n=3^5$
Control experiment	0.25	28.3	0.8	328	33
	0.75	3.7	1.0	310	18
	1.5	8.5	2.2	311	6
	3.5	3.5	0.1	279	1
Fuel cell experiment	0.25	20.4	3.0	239	1
	0.75	25.5	0.8	302	10
	1.25	11.0	1.3	350	31
	2.5	5.6	0.0	345	46
	4.5	4.4	0.1	392	13

Sample	Distance from electrode (cm)	Organic carbon		Total nitrogen	
		Content (weight %)	Standard deviation $n=3^5$	Content (weight %)	Standard deviation $n=3^5$
Control experiment	0.25	3.5	0.2	0.23	0.01
	0.75	5.2	0.4	0.32	0.02
	1.5	5.4	0.1	0.34	0.01
	3.5	4.2	0.1	0.25	0.02
Fuel cell experiment	0.25	2.6	0.3	0.17	0.01
	0.75	2.6	0.2	0.18	0.01
	1.25	3.5	0.0	0.25	0.00
	2.5	4.2	0.1	0.32	0.00
	4.5	4.2	0.4	0.31	0.03

⁵ sediment samples were analyzed in triplicate

Appendix G: Electron microprobe profiles of the active anode surface.

	Distance from the electrode surface (μm)	S wt %	Fe wt %
biofilm	122	0.32	0.00
	111	0.50	0.00
	100	0.42	0.00
	89	0.40	0.00
	78	0.40	0.01
	67	0.54	0.02
	56	0.58	0.02
	44	0.55	0.01
	33	0.63	0.00
	22	0.65	0.01
	11	2.08	1.32
	0	0.09	0.00
graphite	-11	0.03	0.02

	Distance from the electrode surface (μm)	N wt %	Si wt %	P wt %
biofilm	245	2.15	0.03	0.00
	223	1.74	22.96	0.01
	201	5.23	7.66	0.00
	179	4.19	0.02	0.00
	157	1.96	0.13	0.00
	134	1.66	0.45	0.00
	112	3.79	0.05	0.01
	90	5.06	0.03	0.00
	68	3.99	0.03	0.01
	46	3.46	0.05	0.00
	46	3.17	0.05	0.01
	41	4.97	0.09	0.00
	36	2.27	0.02	0.02
	31	1.81	0.61	0.02
	26	2.32	4.27	0.10
	20	1.41	8.60	0.16
	15	0.66	0.24	0.03
	10	1.20	0.23	0.04
	5	0.69	0.21	0.07
	0	0.44	0.08	0.04
graphite	0	0.37	0.08	0.05
	-33	0.65	0.03	0.00
	-66	1.41	0.05	0.01
	-98	1.14	0.01	0.00
	-131	1.54	0.02	0.00
	-164	0.05	0.01	0.00
	-197	0.51	0.01	0.00
	-229	0.90	0.02	0.01
-262	0.62	0.01	0.00	
-295	0.76	0.03	0.00	

	Distance from the electrode surface	N wt %	S wt %	Fe wt %	Si wt %	P wt %
biofilm	246	2.56	0.24	0.00	0.02	0.00
	224	1.87	0.35	0.01	0.09	0.00
	202	1.92	0.32	0.00	0.06	0.01
	179	0.51	0.44	0.00	0.15	0.03
	157	0.11	0.48	0.02	0.09	0.00
	135	0.55	0.21	0.00	40.21	0.00
	113	1.54	0.44	0.01	0.07	0.01
	90	3.75	0.47	0.02	0.02	0.01
	68	3.19	0.49	0.01	0.01	0.00
	46	3.78	0.46	0.03	0.02	0.00
	45	3.13	0.50	0.02	0.01	0.02
	40	4.05	0.47	0.01	0.01	0.02
	35	3.34	0.56	0.01	0.02	0.02
	30	3.12	0.75	0.07	0.15	0.02
	25	2.17	1.43	0.57	1.38	0.04
	20	3.10	1.65	1.02	3.76	0.12
	15	3.65	0.82	0.57	3.53	0.06
10	2.05	0.27	0.07	0.19	0.01	
5	2.01	0.30	0.04	0.03	0.03	
0	2.10	0.40	0.00	0.05	0.02	
graphite	2	2.38	0.45	0.04	0.04	0.04
	-36	0.62	0.07	0.00	0.04	0.01
	-74	0.26	0.03	0.00	0.01	0.01
	-112	0.00	0.03	0.01	0.01	0.01
	-150	0.91	0.06	0.00	0.04	0.00
	-187	0.49	0.08	0.00	0.05	0.02
	-225	0.57	0.02	0.00	0.00	0.01
	-263	0.31	0.02	0.00	0.01	0.00
	-301	0.30	0.02	0.01	0.02	0.01
-339	0.00	0.03	0.00	0.02	0.00	

	Distance from the electrode surface	N wt %	S wt %	Fe wt %	Si wt %	P wt %
biofilm	182	2.10	0.56	0.00	0.10	0.008
	166	1.65	0.58	0.00	0.40	0.000
	149	2.07	0.62	0.03	0.06	0.00
	133	2.06	0.61	0.00	0.08	0.028
	117	1.30	0.63	0.00	0.03	0.001
	100	0.34	0.11	0.02	54.95	0.000
	84	3.18	0.57	0.01	0.18	0.000
	68	2.64	0.61	0.02	0.01	0.008
	51	4.12	0.60	0.00	0.01	0.013
	35	2.34	0.74	0.00	0.03	0.014
	35	1.99	0.77	0.03	0.03	0.010
	31	2.80	0.83	0.00	0.02	0.013
	27	1.12	0.92	0.04	0.08	0.005
	23	0.87	1.46	0.50	1.00	0.067
	19	1.18	1.53	0.77	2.18	0.097
	16	1.50	1.08	0.45	1.36	0.057
	12	0.50	0.40	0.08	0.19	0.030
8	0.14	0.28	0.03	0.07	0.025	
4	0.67	0.26	0.01	0.05	0.000	
0	0.52	0.09	0.00	0.03	0.002	
graphite	0	0.52	0.08	0.02	0.03	0.010
	-27	0.68	0.06	0.01	0.03	0.011
	-55	0.44	0.06	0.01	0.03	0.000
	-82	0.48	0.04	0.00	0.02	0.002
	-110	0.43	0.03	0.01	0.02	0.005
	-137	0.29	0.06	0.19	0.02	0.009
	-165	0.33	0.02	0.02	0.02	0.001
	-192	0.72	0.01	0.00	0.01	0.001
	-220	0.37	0.02	0.01	0.02	0.016
	-247	0.35	0.03	0.01	0.02	0.007
	-275	0.32	0.02	0.00	0.02	0.009
	-302	0.54	0.03	0.02	0.02	0.001
	-330	0.00	0.02	0.13	0.03	0.010
	-357	0.00	0.04	0.07	0.04	0.007
-385	0.32	0.02	0.03	0.01	0.000	

Appendix H: Electron microprobe measurements along the surfaces of active and control electrodes, and Fe/S ratios.

Fuel cell					
Distance along the electrode surface (μm)	S wt %	Fe wt %	S At %	Fe At %	Fe/S (A%)
0	1.75	1.04	0.75	0.26	0.34
980	0.40	0.29	0.16	0.07	0.42
1920	0.56	0.06	0.23	0.01	0.06
3620	1.36	0.72	0.56	0.17	0.30
4980	0.95	0.14	0.39	0.03	0.09
6460	0.40	0.06	0.17	0.02	0.09
9100	0.50	0.10	0.18	0.02	0.11
10900	0.63	0.15	0.24	0.03	0.14
13000	0.23	1.17	0.10	0.29	2.91
12320	0.90	0.31	0.37	0.07	0.20
0	0.73	0.13	0.29	0.03	0.10
137	1.46	0.26	0.68	0.07	0.10
158	1.25	0.37	0.78	0.13	0.17
187	0.89	0.44	0.39	0.11	0.28
212	0.56	0.09	0.25	0.02	0.09
313	1.37	0.60	0.66	0.17	0.25
357	1.33	1.54	0.58	0.39	0.67
407	1.07	0.29	0.46	0.07	0.15
627	1.26	0.24	0.56	0.06	0.11
1290	1.21	0.98	0.47	0.22	0.47
1736	0.96	0.10	0.56	0.03	0.06
1751	0.91	0.35	0.45	0.10	0.22
1833	0.59	0.13	0.31	0.04	0.13
1865	0.56	0.03	0.28	0.01	0.03
2490	0.69	0.05	0.32	0.01	0.04
2565	0.35	0.04	0.14	0.01	0.07
2677	0.66	0.09	0.34	0.03	0.08
6740	0.66	0.10	0.27	0.02	0.08
10200	0.36	0.02	0.16	0.00	0.03
10264	0.94	0.48	0.42	0.12	0.29

Control cell					
Distance along the electrode surface (μm)	S wt %	Fe wt %	S At %	Fe At %	Fe/S (A%)
3729	0.124	0.025	0.053	0.006	0.114
3805	0.081	0.000	0.037	0.000	0.000
3944	0.021	0.003	0.009	0.001	0.074
5943	0.068	0.011	0.038	0.004	0.094
6035	0.056	0.000	0.025	0.000	0.000
6921	0.051	0.005	0.022	0.001	0.055
8680	0.009	0.018	0.004	0.005	1.175
9115	0.072	0.005	0.031	0.001	0.039
9248	0.112	0.003	0.050	0.001	0.014
9331	0.064	0.000	0.029	0.000	0.000
9819	0.089	0.019	0.038	0.005	0.123
9911	0.023	0.000	0.010	0.000	0.000
10336	0.053	0.000	0.025	0.000	0.000
11482	0.071	0.002	0.030	0.001	0.017
12383	0.093	0.017	0.042	0.004	0.106
12499	0.050	0.022	0.023	0.006	0.248
12578	0.051	0.004	0.022	0.001	0.041
12635	0.025	0.000	0.010	0.000	0.000
13075	0.024	0.000	0.010	0.000	0.000
13361	0.030	0.003	0.013	0.001	0.056
14042	0.038	0.012	0.017	0.003	0.184
14101	0.028	0.000	0.013	0.000	0.000
15782	0.069	0.018	0.031	0.005	0.150
584	0.058	0.006	0.025	0.001	0.057
537	0.104	0.010	0.052	0.003	0.057
188	0.060	0.001	0.028	0.000	0.011
93	0.041	0.000	0.019	0.000	0.000
0	0.041	0.000	0.017	0.000	0.000